

The Volyn biota (Ukraine) – 1.5 Ga old eukaryotes in 3D- preservation, a spotlight on the ‘boring billion’

Gelöscht: (micro)fossils

Gerhard Franz¹, Vladimir Khomenko², Peter Lyckberg³, Vsevolod Chournousenko⁴, Ulrich Struck⁵, Ulrich Gernert⁶, Jörg Nissen⁶

¹Institut für Angewandte Geowissenschaften, Technische Universität Berlin, D-10587 Berlin, Germany

²M.P. Semenenko Institute of Geochemistry, Mineralogy and Ore Formation, The National Academy of Sciences of Ukraine, 34, Palladina av., Kyiv, 03142, Ukraine

³Luxembourg National Museum of Natural History, 25 Rue Münster, 2160 Luxembourg, Luxembourg

⁴Volyn Quartz Samotsvety Company, Khoroshiv (Volodarsk-Volynski), Ukraine

⁵Museum für Naturkunde, Leibniz-Institut für Evolutions- und Biodiversitätsforschung, Invalidenstraße 43, Berlin, D-10115, Germany

⁶Zentraleinrichtung Elektronenmikroskopie, Technische Universität Berlin, D-10623 Berlin, Germany

Correspondence to: Gerhard Franz (gefra548@gmail.com; gerhard.franz@tu-berlin.de)

Feldfunktion geändert

Abstract

The Volyn biota, fossilized organisms with a minimum age of 1.5 Ga, were found in cavities in granitic pegmatites from the Korosten pluton, NW Ukrainian shield. Fossilization was due to influx of hydrothermal fluorine-rich waters, which silicified the outermost part of the organisms, thus preserving the 3D morphology. Details of the morphology (investigated by scanning electron microscopy) show that the majority of the specimens is filamentous, of a large variety with diameters ranging from ~10 µm to ~200 µm, thin filaments with typical branching, thick filaments with ball-shaped outgrowths and dented surface. Filaments can be straight or conical, curvilinear or strongly curved, up to mm in length, some with a central channel. Some filaments show indications for segmentation, are grown as sessile organisms onto substrate; others show both intact ends, indicating growth in soft medium or planktonic organisms. Objects with flaky morphology and agglutinating filaments are interpreted as fossil biofilms. Other objects are hollow and show a large variety of forms; spherical objects are scarce. Infrared spectroscopy indicates the presence of chitosan in one filament type, electron microprobe analysis of nm-sized inclusions in filaments identified the presence of Bi(Te,S)

Gelöscht: floating

Gelöscht: in water

38 minerals, and both observations are compatible with the interpretation as fungi-like organisms.
39 Stable C- and N-isotope data of bulk samples are in the range of -31 to -47 ‰ $\delta^{13}\text{C}_\text{p}$ and
40 of +3 to +10 ‰ $\delta^{15}\text{N}_\text{p}$ indicating possible methanogens as part of the subsurface micro-
41 ecosystem. The Volyn biota show that at 1.5 Ga eukaryotes including fungi-like organisms
42 lived in the continental deep biosphere, where complex forms of life existed, well above the
43 microscopic level.

Gelöscht: of filaments

Gelöscht: ^{12}C

Gelöscht: ^{14}N

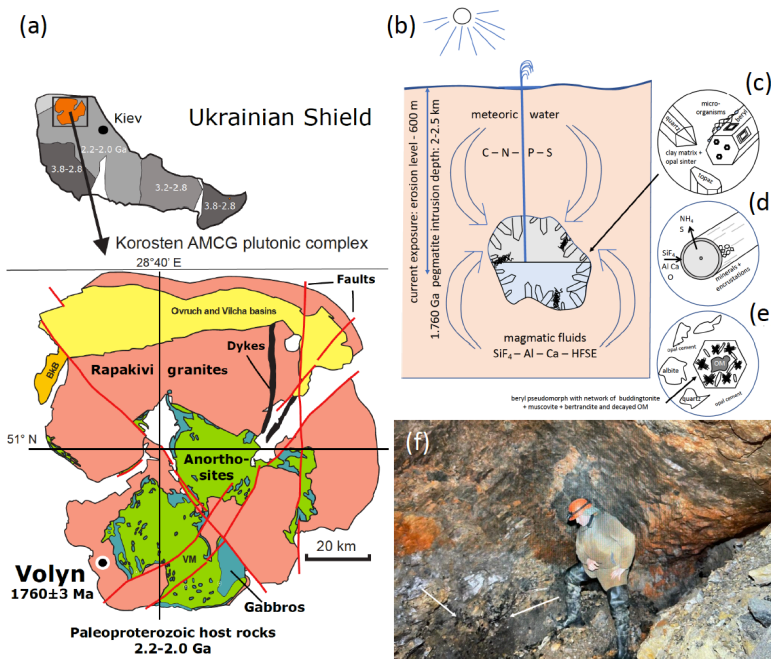
Gelöscht: ic bacteria

46 1 Introduction

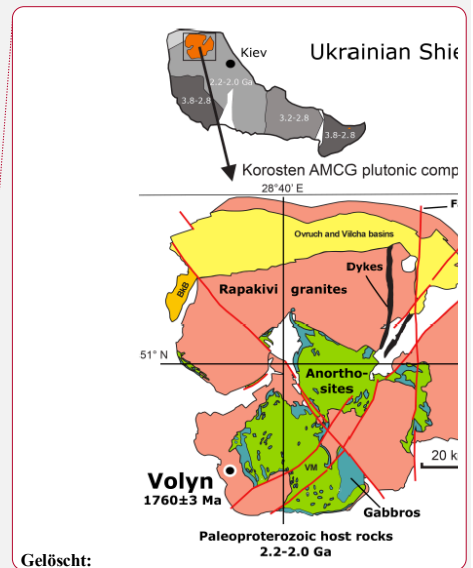
47 Precambrian fossils are generally not well preserved because of the absence of skeletal parts.
48 In addition, most Precambrian fossil record is from sedimentary rocks with strong diagenetic
49 or even metamorphic overprint, which destroyed much of the original morphology and in
50 extreme cases of very old organisms left only an isotopic signature (e.g. Alleon et al., 2018;
51 Berbee et al., 2020). Therefore, their biogenicity is often disputed especially when the organic
52 matter (OM) is completely replaced, often by silica or pyrite. A preservation of 3D-morphology
53 is very rare and requires special fossilization conditions, which include first prevention of rapid
54 decay of the OM and then preservation of the space around the fossil in order to preserve its
55 original morphology. These conditions were fulfilled in pegmatites of the Volyn pegmatite
56 field, Ukraine, associated with the Korosten Pluton. These so-called ‘chamber pegmatites’
57 contain large miarolitic cavities in which OM named (oxy)-kerite was found and in previous
58 investigations interpreted as an example of a-biogenic formation (Ginzburg et al., 1987;
59 Luk’yanova et al., 1992), later re-interpreted as fossil cyanobacteria (Gorlenko et al., 2000;
60 Zhmur, 2003) from a geyser type deposit. Ginzburg et al. (1987) give a composition of 60-76
61 wt% C, 5-7 wt% H, 9-23 wt% O, 8-9 wt% N, and 2-3 wt% S and an empirical formula of
62 $\text{C}_{491}\text{H}_{386}\text{O}_{87}(\text{S})\text{N}$. Gorlenko et al. (2000) and Zhmur (2003) mention masses of up to 3 kg of
63 kerite in one of the cavities with an irregular distribution within the pegmatite.

64 The organisms lived in these cavities and provide an example of the Precambrian deep
65 biosphere. Their fossilization conditions included sudden influx of hot hydrothermal waters in
66 the geyser system, where magmatic fluids rich in SiF_4 mixed with meteoric waters (Franz et al.,
67 2022a), infiltration of Si-Al into the outermost layer of the fossils, and formation of dominantly
68 clay mineral encrustations. The 1.76 Ga intrusion age of the pegmatites (U-Pb zircon;
69 Shumlyanskyy et al., 2021) provides a maximum age of the fossils; the minimum age of 1.5 Ga
70 is provided by the age of formation of a breccia, which contains degraded OM, brown opal with
71 OM, buddingtonite which NH_4 -content was provided by the degraded OM, and muscovite

76 (^{40}Ar - ^{39}Ar laser ablation data; Franz et al., 2022b). An additional argument for this age comes
 77 from the brown opal, which cements the breccia and contains organic matter (Franz et al., 2017,
 78 and references therein). Therefore, we assume that breccia formation must have occurred when
 79 organic matter was already present in the ‘chambers’. Although some of the miarolitic
 80 chambers collapsed, producing the muscovite-opal-bearing breccia, other chambers are still
 81 intact and were mined since the 1930ies for piezo quartz and until now for pegmatite minerals
 82 such as beryl and topaz (Ivanovich and Alekseevich, 2007; Lyckberg et al., 2009, 2019).
 83 We report here details about the morphology and the internal structure of the fossils,
 84 investigated by scanning electron microscopy (SEM) and electron microprobe analysis
 85 (EMPA), and provide stable C-N isotope and infrared spectroscopy (FTIR) data, which allow
 86 speculating about the types of organisms. An important point is that these ‘micro’-fossils in
 87 many cases reach a size well above the microscopic level, with filaments of several mm in
 88 length. The age of the fossils of 1.5 Ga in the middle of the ‘boring billion’ and gives insight
 89 into the organisms of the deep continental biosphere.



90
 91 **Fig. 1 (a) Location of the Volyn pegmatite field in the Ukrainian shield, which hosts the**
 92 **Volyn biota. (b) Conceptual model for the fossilization in the miarolitic cavities**
 93 **(‘chambers’) in the pegmatite. Current exposure is from the erosion level to a depth of**
 94 **600 m. Kerite is attached to the walls, often to feldspar, but also (c) on topaz and beryl**



crystals. (d) Fossilization produces a thin rim of Si-Al enrichment and encrustations of clay minerals. (e) In collapsed chambers, a breccia formed with pseudomorph of buddingtonite+muscovite+opal after beryl. Decaying kerite produced NH_4 for formation of buddingtonite. The Ar-Ar-LA age of muscovite is considered as minimum age for the fossils. (f) View into a chamber, arrows point to black kerite; (all images reproduced from Franz et al., 2022a).

2 Geological framework and sample material

The locality in the Ukrainian Precambrian shield is associated with the Korosten anorthosite-mangerite-charnockite-granite plutonic complex (Shumlyanskyy et al., 2012) (Fig. 1). The samples were recovered from underground in shaft 3 of the mine from a depth of approximately 100 m, one sample was obtained from the mineralogical museum of the Academy of Sciences, Kiev, and one beryl sample with kerite on beryl was collected from the mine tailings (Table 1). Two additional samples of topaz from the museum in Kiev with kerite (Fig. 2) were not investigated in detail. The samples from underground could be simply picked up with no need for separation from rock matrix and were stored in plastic sample bags. Kerite has not been found outside the cavities, which are in the core of the pegmatite. It exists as fine fiber masses between fragments of the wall of the cavities and as larger masses hanging freely on the walls, attached to feldspar and often around topaz (Fig. 2b, c) and to beryl (Fig. 2d-j). The bottom of the cavities is covered with soft clay.

Formatiert: Schriftart: Nicht Fett, Nicht Kursiv

Formatiert: Schriftart: Nicht Fett, Nicht Kursiv

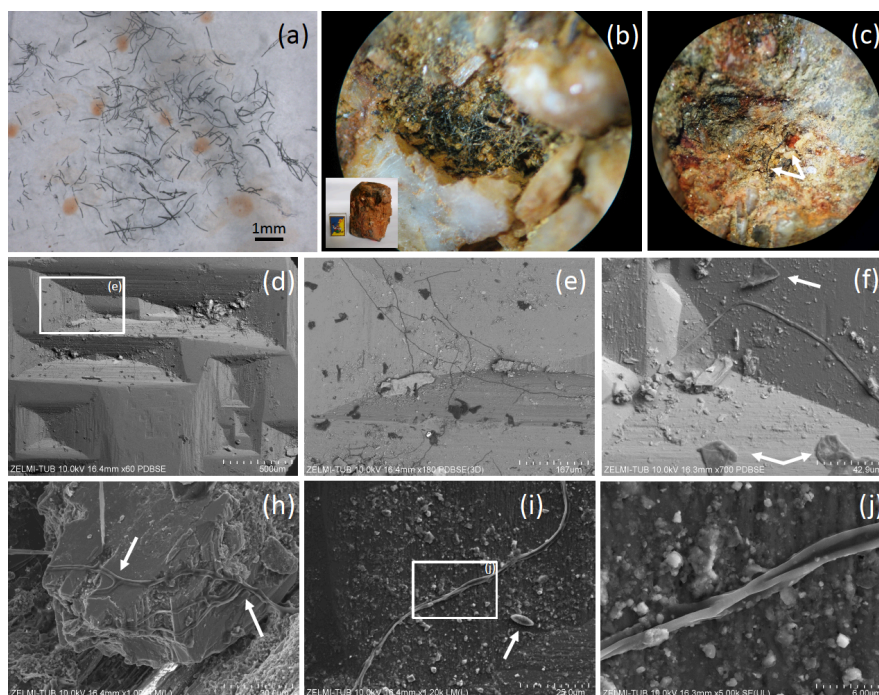


Fig. 2 (a) Photograph of sample #0, illustrating the pieces of broken, solitary kerite filaments of mm-length. (b) Photograph of kerite filaments on topaz (white crystals with Fe-oxide-hydroxide staining; inset shows topaz crystal with 5-cm large matchbox for scale, image diameter approximately 2 mm). (c) Filaments of different diameter on topaz (arrows; image diameter approximately 3 mm). (d) SEM image (with combined back scattered mode) of beryl prism surface with characteristic etch pits. Rectangle indicates position of (e), which shows filamentous kerite together with kerite in irregular shape (dark contrast indicates organic matter). (f) SEM image, arrows point to kerite with irregular shape. (h) Kerite filaments with branching (arrows) in dissolution feature of beryl. (i) Kerite filament and spherical kerite (arrow) in an etch pit of beryl; rectangle indicates position of (j), illustrating the irregular diameter of the filament.

The sample #0 consists of broken filaments of several mm length (Fig. 2a) and it is likely that the original length was much larger on the cm scale. It was also found grown onto a topaz crystal (Fig. 2b, c). On beryl it was found attached to dissolution features on the surface of the crystals, but not only in the common filamentous form, but also in irregular shape (Fig. 2d-j) and rarely in spherical shape (Fig. 2i). Although the previous reports mention mostly filaments with smooth surface, our new observations revealed a large variety of different types of filaments, described below.

3 Methods

The samples were investigated by SEM and EMPA. SEM images were obtained with a Hitachi SU8030 instrument, equipped with an EDAX EDS system with a 30 mm² silicon drift detector (SDD) fitted with a silicon nitride window. Samples were coated with an approximately 5 nm thick Ir layer allowing for high-resolution imaging of the filaments' surfaces without the structure of commonly applied Au coating. The kerite samples without further cleaning or preparation were mounted on Al stubs stickered with conductive carbon tabs. The beryl crystals with kerite filaments were dust-cleaned with compressed air and coated with C.

145

Table 1: List of samples

No./GFZ no.	Year of sampling	Material	Location
0/Museum Ac. Sci. Kyiv	unknown	kerite	unknown
1/G017809	2018	kerite	shaft 3
2/G017810	2018	kerite	shaft 3
3/G017811	2018	kerite	shaft 3
4/G017812	2018	kerite	shaft 3
5/G017813	2013	kerite	shaft 3
6/G017814	2013	kerite	shaft 3
7/G017815	2013	kerite	shaft 3
2008-V-10	2008	beryl crystal with etch pits	mine tailings pegmatite #2

147

The JEOL JXA-8530F field emission electron microprobe at TU Berlin was used to investigate mounts embedded in epoxy, but with C-coating, for quantitative results and less absorbance (compared to Ir). EPMA data for element distribution maps of cross sections or of parts of the rim of the filaments and flaky kerite were acquired in the wave-length dispersive mode using an 8 kV, 20 nA beam with a probe diameter of 64 nm. Back-scattered electron images (BSE) were taken to select appropriate sites. Mappings were done in stage scan-modus with pixel resolution between 277 and 360 x 180 and 265, with a pixel size of mostly 80 nm, and a dwell time per pixel of 200 ms. Total scan areas varied between 70 x 36 µm to 33.2 x 31.8 µm.

Stable isotope analysis and concentration measurements of nitrogen and carbon were performed simultaneously with a THERMO/Finnigan MAT V isotope ratio mass spectrometer, coupled to a THERMO Flash EA 1112 elemental analyzer via a THERMO/Finnigan Conflo IV- interface in the stable isotope laboratory of the Museum für Naturkunde, Berlin. Isotope ratios are expressed in the conventional delta notation ($\delta^{13}\text{C}$ / $\delta^{15}\text{N}$) relative to atmospheric N (Mariotti, 1983) and VPDB (Vienna PeeDee Belemnite standard). Standard deviation for repeated

162 measurements of lab standard material (peptone) is generally better than 0.15 per mill (‰) for
163 both N and C. Standard deviations of concentration measurements of replicates of our lab
164 standard are <3% of the concentration analyzed.

165 FTIR absorption spectra of several small, 40-60 µm wide, translucent dark-brown fragments of
166 kerite (sample #0, which showed the least mineralization crust) were measured in the spectral
167 range 7000 – 700 cm⁻¹ at room temperature using a Bruker IFS 66 spectrometer equipped with
168 an IR-microscope. The kerite fragments were selected under a binocular microscope and placed
169 on an IR-transparent KBr plate. Spectra were taken in the transmittance mode at a spectral
170 resolution of 4 cm⁻¹ with a measuring spot diameter of 40 µm. The reference spectra were
171 measured through the same KBr plate. The time-averaged signal was collected over 200 scans
172 in both reference and sample spectra. For comparison, absorption spectra of chitin (poly-(1,4)-
173 β-N-acetyl-D-glucosamine) and >75% deacetylated chitin, or chitosan (2-amino-2-deoxy-
174 (1,4)-β-D-glucopyranan, both produced by Sigma-Aldrich Chemie GmbH (C7170-100G,
175 C3646-10G) from shrimp shells, were measured in several single flattened, 30-50 microns thick
176 transparent flakes of these materials at the same conditions. Band assignments are based on
177 literature comparison (Table 1 Supplement).

178 4 Results

179 4.1 Morphology

180 4.1.1 Filaments

181 Filaments are curvilinear with smooth surfaces and circular cross section (Fig. 3) with different
182 types of ends (Fig. 4). Other types have a structured surface, some are conical, others strongly
183 curved (Figs. 5, 6). Branching is typical for filaments with smooth surface, and was observed
184 as Y-, T-, and double-T-branching (Fig. 3b, h), as multiple branching (Fig. 3c), and combined
185 Y-T-branching (Fig. 3d). Clear indications for anastomosing filaments were not found. Multiple
186 branching represents the beginning of growth of filaments (Fig. 3e). In others, globular
187 outgrowths possibly mark the beginning of new branches (Fig. 3g). Whereas the diameter of
188 the individual filaments can be homogeneous between approximately 10 µm and 20 µm (sample
189 #0), others (e.g. sample #3; Fig. 3f) show different diameters, between a few µm and several
190 tens of µm. Ball-shaped outgrowths at the end of a filament occur together with a conical
191 thinning-out filament (sample #1; Fig. 3i). Conical, thinning out filaments originate in Y-
192 branching from a thicker filament with constant diameter (Fig. 3m). One object was identified
193 with multiple conical filaments, with claw-like curved ends (sample #6; Fig. 3j, k, l). The
194 bottom part can be interpreted as beginning of growth of the filaments on a substrate, i.e. the
195 clay mineral assemblage in the miarolitic cavities.

Gelöscht:

Most filaments are broken pieces of larger filaments, and preserved length is in the order of mm, and it can be assumed that the original length was up to cm. Complete filaments were observed, with one end ball-shaped, the other end thinning out (Fig. 6i, o). Whereas beginning of a filament is rarely observed, ends are frequently preserved (Fig. 4) and can be either simply round (Fig. 4a), ball-shaped (Fig. 4b-f), rarely with oval shape (Fig. 4e), or conical-thinning out (Fig. 4g, l, m).

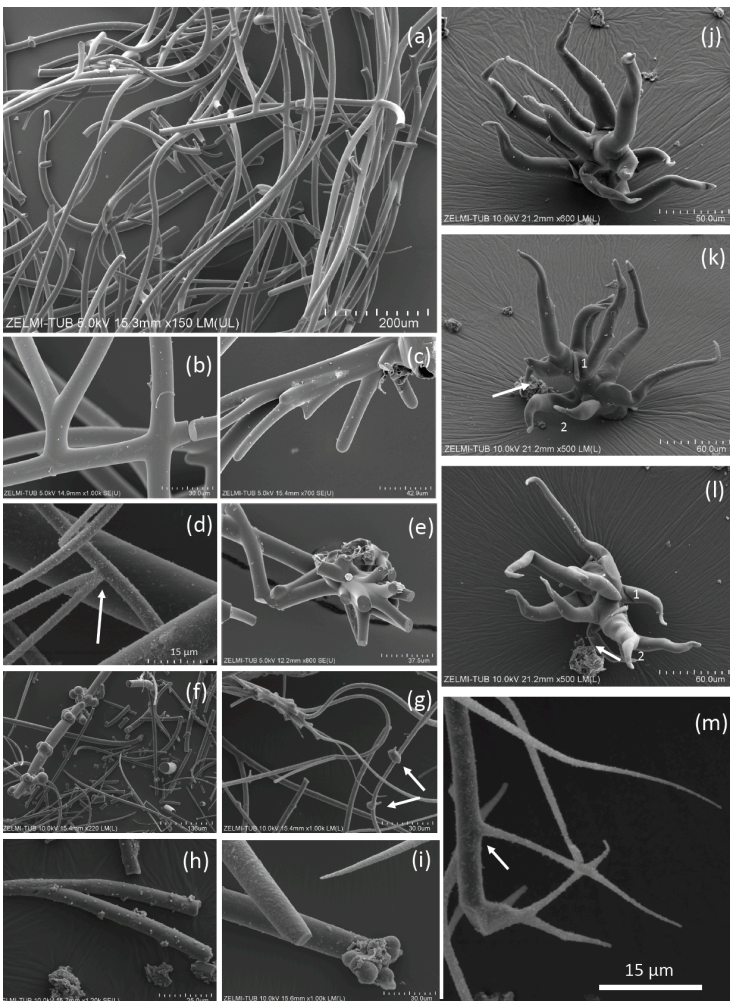


Fig. 3 SEM images of curvilinear filaments with smooth surfaces and circular cross section. (a) Overview of sample #0, illustrating the amount of material with homogeneous diameter of approximately 10 μm, length of more than 1 cm, round ends. (b) Branching with Y-, T- and double-T-junctions. (c) Multiple branching and (d) combined Y- and T-

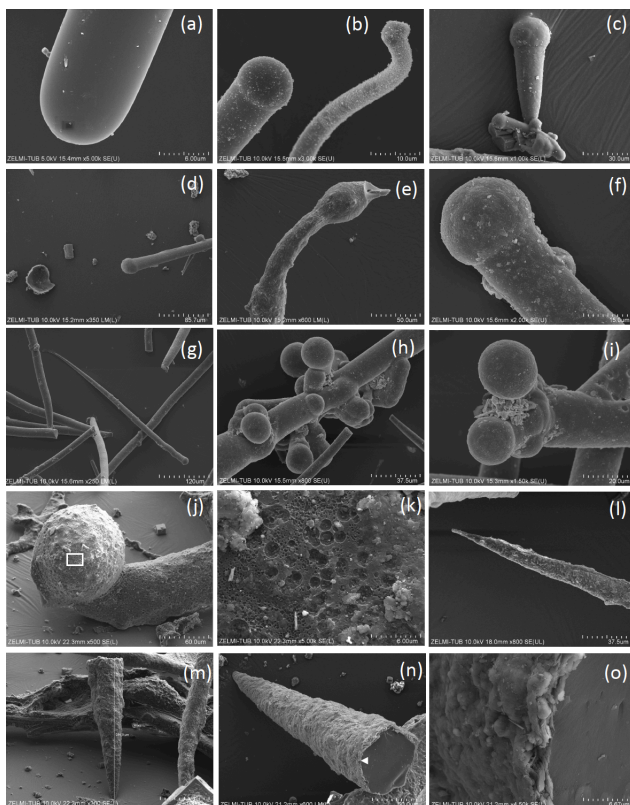
branching. (e) Possible multiple branching representing the beginning of the filaments. (f) Overview (sample #3) with filaments of variable diameter and (g) multiple branching (upper left) and small outgrowths (arrows). (h) Sample #4 with Y-branching. (i) Sample #1 showing 3 filaments, one thinning out (upper left), one with constant diameter with ball-shaped outgrowths on end (below), and a slightly conical one (above). (j, k, l) Image of multiple, conical filaments with claw-like ends, growing from a common center; view of the same object (sample #6) in different perspectives. In (k) and (l) numbers 1 and 2 identify the same beginning and end of a filament; arrows point to a fluorite crystal. (m) Y-branching of a thinning-out filament (arrow) starting from a filament with constant thickness. The star-like shape in the center is not branching, it shows different filaments in different heights.

Ball-shaped outgrowths (Fig. 4h) and multiple ball-shaped ends (Fig. 4i) possibly mark the beginning of new branches, and balls can be situated asymmetrically at the end of a filament (Fig. 4j). The structured surface of this ball-shaped end is caused by the fossilization process, as indicated by the round pores in the surface, together with mineral incrustations (Fig. 4k). This is also seen on the surface of a 300 μm long conical filament fragment (Fig. 4m, n), which has a μm -wide rim of mineral incrustations with a homogeneous interior part (Fig. 4o).

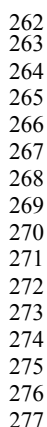
The structured surface is only partly a result of the fossilization process. Figure 5a-f shows a filament with approximately 4 mm preserved length and oval cross section (120x80 μm thick on one end), which has a dented surface and bulbous outgrowths (Fig. 4d). Another example of a strongly curved filament (Fig. 4g-l) with bulbous surface, several mm in length and near to 200 μm diameter shows irregular segmentation in distances between 35 μm and 70 μm . On the surface of the filament, relicts of a sheath are visible, partly the sheath is intact. The transition between the intact sheath and the remnants exhibits a polygonal structure and circular 1-2 μm wide holes, probably caused by decay/fossilization. Segmentation is also seen in a branched filament with approximately 3-5 μm wide ridges (Fig. 4m, n, o). This filament has a mineralized outer part of clay minerals with irregular ridges; however, where branching starts, the surface is intact. We interpret these irregular ridges as irregular segmentation of the filament, accentuated and emphasized by fossilization.

Some samples have joint occurrence of filaments with smooth, slightly, and strongly bulbous surfaces (Fig. 6a, b), and joint occurrence of straight, slightly, and strongly curved filaments with irregular segmentation (Fig. 6c, d). The strongly bulbous filaments are transitional to outgrowths (Fig. 6d). Segmentation is indicated (Fig. 6e) and the surface can be strongly sculptured. The filaments have variable diameters from 75 μm (Fig. 6e) to approximately 250 μm (Fig. 6d, f). Some thin filaments show clear indication for segmentation (Fig. 6g, h). The strongly sculptured surface consists of small ball-shaped outgrowths. Joint occurrence of

245 filaments with strongly sculptured surface and smooth surface and with slight striation
 246 perpendicular to filament length, and filaments with strong sculptured surface (Fig. 6k, l, m, n),
 247 indicates that these are probably different types of organisms, not different stages of
 248 fossilization.



249 **Fig. 4 SEM images of ends of filaments with smooth surface. (a) Simple round end (sample**
 250 **#0). (b) Ball-shaped end of straight and curved filament (sample #3). (c) Ball-shaped end**
 251 **of conical filament (sample #1). (d) Ball-shaped end of straight filament (sample #5). (e)**
 252 **Oval-shaped outgrowths near end of filament (sample #7). (f) Ball-shaped end (sample**
 253 **#1). (g) Complete filament with one end thinning out, one with a round end (sample #1).**
 254 **(h) Ball-shaped outgrowths and ends (sample #3). (i) Double ball at end of filament**
 255 **(sample #1) (j) Ball-shaped end; rectangle indicates position of (k), surface of the ball with**
 256 **mineral incrustations and porosity, interpreted as result of decay/fossilization (sample**
 257 **#6). (l) Thinning-out of a filament (sample #5). (m, n) Cone-shaped filament in different**
 258 **perspective, approximately 300 μ m preserved length (sample #6); white rectangle**
 259 **indicates position of (o) detail of the 1-2 μ m wide rim with mineral incrustations.**
 260
 261



11

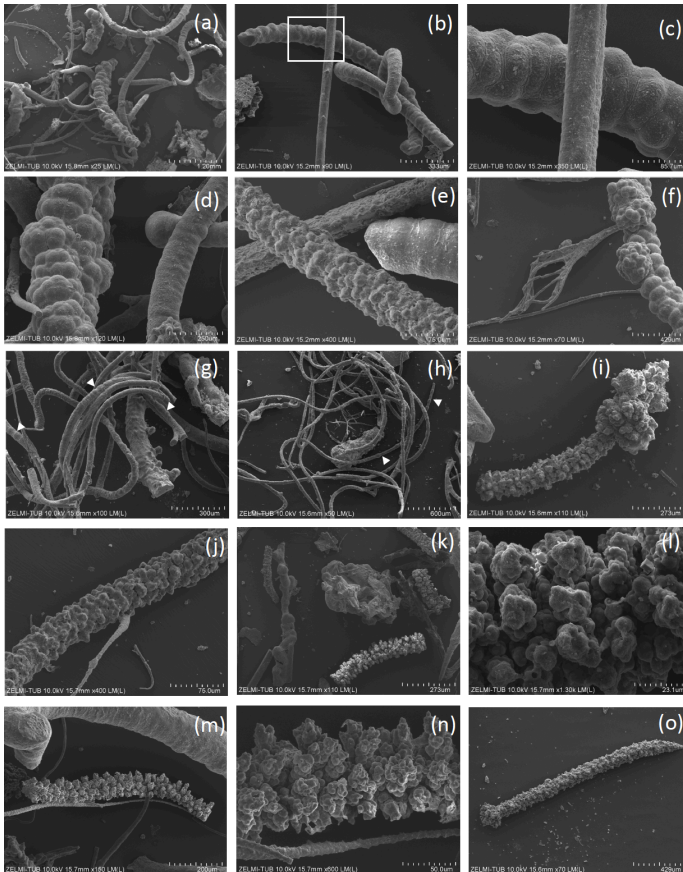


Fig. 6 SEM images of filaments with structured, rough surface 2. (a) Overview illustrating joint occurrence of smooth, slightly, and strongly bulbous surfaces (sample #5). (b) Joint occurrence of straight, slightly and strongly curved filaments; rectangle indicates detail in (c) with irregular segmentation of the slightly curved filament. The straight filament also shows a slight structure on the surface (lower right). (d) Joint occurrence of slightly bulbous (right) and strongly bulbous filaments, transitional to outgrowths. (e) Filament with indication for segmentation (right) and filament with strongly sculptured surface; note small diameter (75 μ m) compared to the large filament in (d). (f) Thick filament with bulbous outgrowths, next to thin agglutinated filaments. (g, h) Thin filaments with indication for segmentation (white triangles). (i) Complete filament of approximately 1 mm length with strongly sculptured surface and outgrowths. (j) Part of a filament with strongly sculptured surface. (k) Joint occurrence of filaments with strongly sculptured surface and smooth surface, together with and irregularly shaped object (center). (l) Detail of strongly sculptured surface, which consists of small ball-shaped outgrowths. Note fluorite crystal in upper right, below label (m), which shows joint occurrence of thick filament (top) with slight striation perpendicular to filament length, and filament with strong sculptured surface, detail shown in (n). (o) Almost 2 mm long complete filament, one thin end, one with outgrowths.

297

298 **4.1.2 Hollow objects**

299 Some objects appear hollow (Fig. 7); one object (Fig. 7a, b) has a hollow lower part transitional
300 into a more solid upper, strongly bulbous part. The hollow rather irregular objects (Fig. 7c)
301 occur together with filaments. Filaments can be also hollow (Fig. 7d-h) and the thickness of the
302 outer rim is approximately 2 μm (Fig. 7h). This is the width of the fossilized outer part of
303 filaments, which we documented in the previous study (Franz et al., 2022a) and therefore we
304 interpret the hollow objects as organisms in which the interior part was completely decayed
305 during and after the fossilization process. Some of the hollow objects are bowl-shaped (Fig. 7i-
306 n). One such object (Fig. 8) is >1 mm large and from the view in different perspectives is can
307 be seen that it is grown onto mineral substrate; next to the clay minerals fluorite is a
308 characteristic mineral and indicates a high fluorine activity in the fossilizing fluid (Franz et al.,
309 2022a). The base of mineral substrate is followed by an approximately 10 μm thick solid rim
310 with bulbous outgrowths.

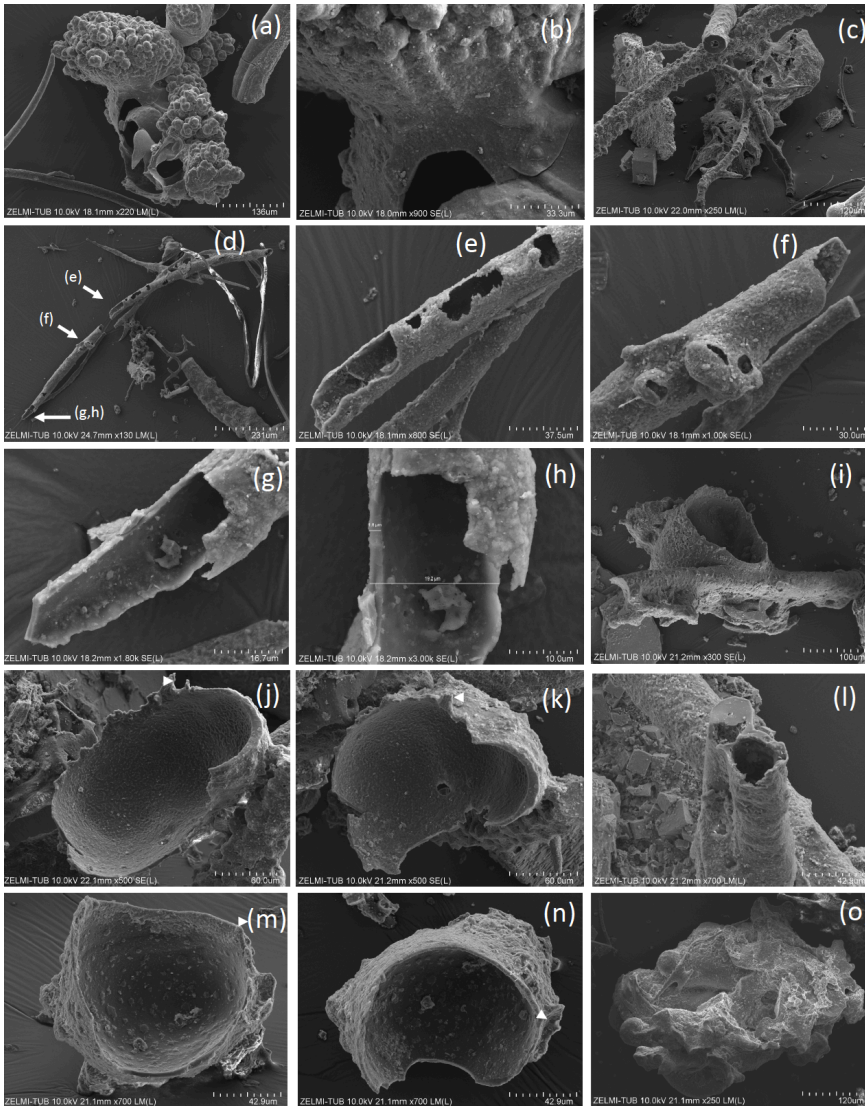
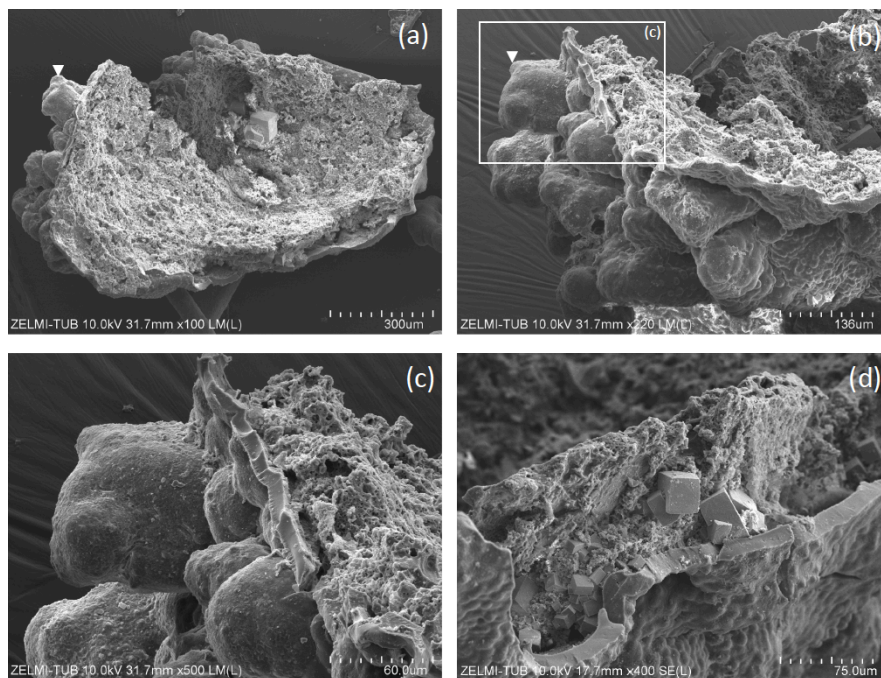


Fig. 7 SEM images of hollow objects. (a) Irregular-bulbous base of a strongly sculptured object, with (b) detail of the transition (center in (a); sample #5). (c) Irregular hollow object below filaments (sample #6). (d) Hollow filament, approximately 1 mm preserved length; position of enlarged parts in (e-h) is indicated (sample #5). The mineralized rim is 1-2 μm wide, diameter near 20 μm . (f) Bulbous outgrowths are also hollow. (i) Filament with an attached hollow form, similar to outgrowths, but much larger (sample #6). (j, k) Same object as in (i), enlarged in two different perspectives; white triangle indicates identical point. (l) Hollow filament next to a filament with a central channel (sample #6). (m, n) Isolated hollow bowl-shaped object in two different perspectives; white triangle indicates identical point (sample #6). (o) Irregular object, partly hollow (sample #6).

322



323

324 **Fig. 8 SEM images of >1 mm large bowl-shaped object (sample #5) (a) seen from below,**
 325 **grown onto mineral substrate; euhedral crystal is fluorite, white triangle indicates**
 326 **position of (b), enlarged part of the rim. Rectangle indicates position of (c) illustrating the**
 327 **base of mineral substrate (right) followed by an approximately 10 μm thick solid rim with**
 328 **bulbous outgrowths. (d) Detail of the solid rim with several fluorite crystals.**
 329

330 4.1.3 Spherical objects

331 Most spherical objects (Fig. 9) appear as rather complete, with only some parts broken off. One
 332 object with a double-ball shape (Fig. 9a,b) is clearly grown onto the substrate (Fig. 9c). The
 333 double-ball with remnants of a sheath points to cell separation. Note the different size of the
 334 objects from < 10 μm (Fig. 9m) to > 1 mm (Fig. 9g). Two small objects identified on the etched
 335 beryl surface appear like seeds or spores (Fig. 9l, m).
 336

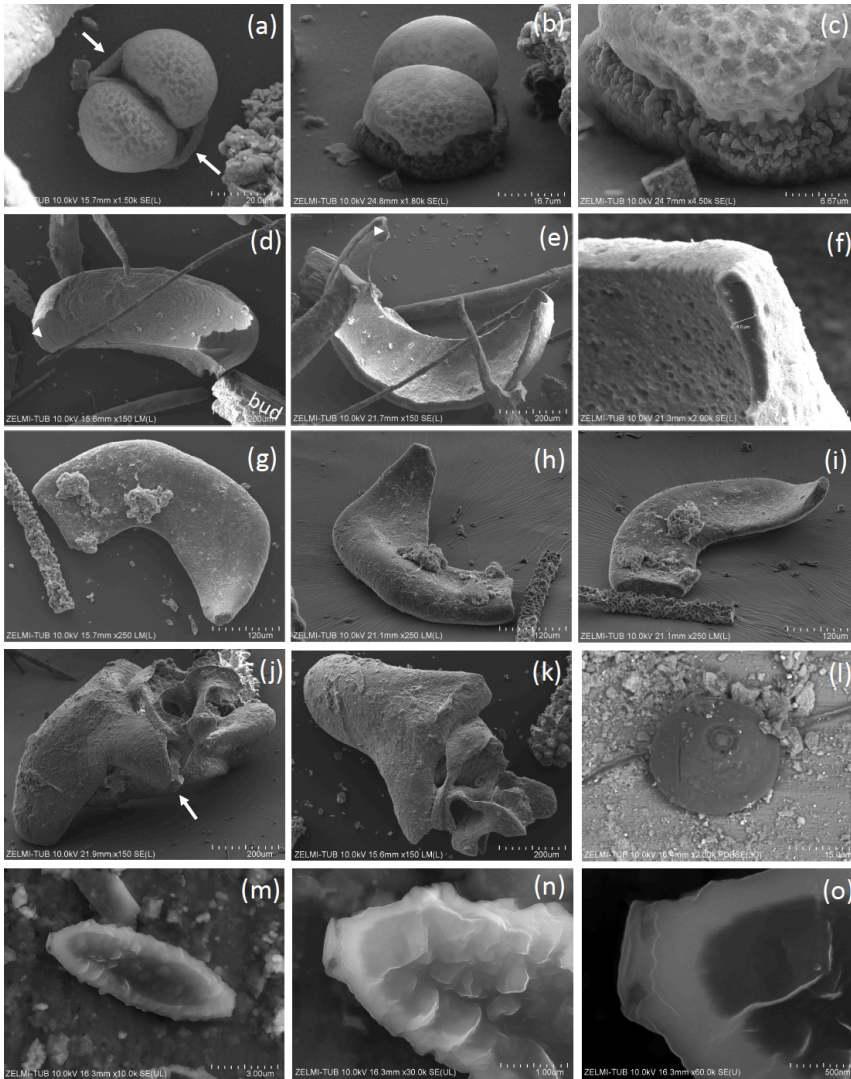


Fig. 9 SEM images of spherical objects. (a, b, c) Same object in different perspective and magnification; arrows in (a) point to a sheath; the euhedral crystal in (c) is fluorite. The object growth from a flat mineral surface into a double-ball with dented surface. (d, e) Same object in different orientation; white triangle indicates identical position; bud = buddingonite. (c) The thickness measured at one point is approximately 6 μm . (g, h, i) Approximately 0.5 mm large object in different perspective with mineral incrustations. (j, k) Irregular, partly hollow object in different perspective. (l) Perfectly round object, sitting on a filament, on etched surface of beryl (compare Fig. 2d); the circular round structure on its top is beam damage. (m, n, o) Oval object on etched surface on beryl (compare Fig. 2i). The lower contrast (dark) in the central part indicates less dense (partly hollow) material.

349 4.1.4 Irregular objects

350 Irregular, flaky objects are abundant, especially on the surface of the beryl crystal (Fig. 2e, f),
351 but also in many samples (e.g. Fig. 6k, 7a, c, o, 8, 9j, k). They show the same fossilization
352 features as the filaments with a thin rim enriched in Si, Al, Ca, and P, loss of N, and oxygenation
353 (Franz et al., 2022a). In some samples (Fig. 6f) filaments appear agglutinated by OM and we
354 interpret these as well as the irregular objects on the beryl crystals as fossilized biofilm.

355 4.2 Internal structure

356 For investigation of the internal structure we used SEM images of broken filaments and other
357 objects, as well as polished sections embedded in epoxy, investigated by BSE images including
358 mapping of element distribution. Data of open-pyrolysis and TEM data (Franz et al., 2022a)
359 had shown that the OM is highly mature, amorphous oxy-kerite. Indications for an outer cell
360 wall are absent, because the outer rim of the fossils is silicified, partly with formation of mineral
361 incrustations.

362 Segmentation of filaments, which might be a characteristic phenomenon for certain organisms
363 and is observed in the filaments' morphology (Figs. 5g, h, 6b, c, e, h) is not obvious in cross
364 section, but one section shows internal cracks, separating the filament in ~50 µm to 100 µm
365 wide segments (Fig. 10a, b). A section of a bulbous fossil shows cracks, which separate the
366 individual bulbs from each other (Fig. 10g, h).

367 The outer rim of the filament shows the typical enrichment of Si and Al (Fig. 10b), and the
368 inner, homogenous and not silicified part shows abundant, nm-sized mineral inclusions (Fig.
369 10c). They are located in the central part and thus not related to the fossilization process,
370 irregularly distributed or in linear array of several crystals (Fig. 10e, h). The minerals were
371 analyzed with the EDS-system and due to their small size in the order of a few nanometers,

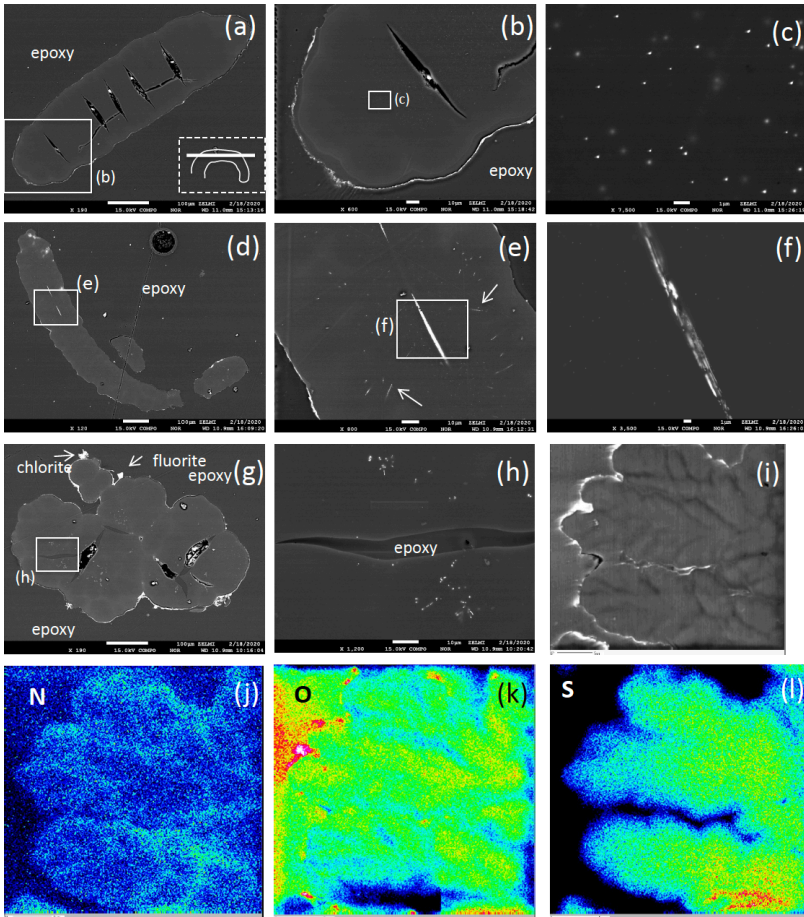


Fig. 10: BSE images of filamentous (a-f) and bulbous fossils (g, h, i), embedded in epoxy, polished thin section and element distribution (j, k, l). (a) Part of curved filament; orientation of section is shown in rectangle (dashed lines), position of enlargement (b) in rectangle (solid lines). Open cracks (black contrast, with impurities from polishing material) indicate approximately 50 μm to 100 μm wide segments. (b) Silicified outer rim (white contrast, irregular) and a narrow, up to 10 μm wide inner rim, are interpreted as effect of fossilization. The homogeneous appearing central part shows in the enlarged image (c) irregularly distributed inclusions, tens of nm in size, of Bi-S-Te minerals. (d) Filament with two, central oriented Bi-S-Te mineral inclusions, approximately 50 μm in length and 1-2 μm wide, enlarged shown in (e) and (f). Arrows in (e) point to straight aligned inclusions, and (f) shows irregular contrast, possibly caused by heterogeneous distribution of Fe and Cu in the Bi-S-Te minerals. (g) Bulbous fossil, with silicified rim and encrustations of chlorite and fluorite. Cracks, partly filled with epoxy, separate individual bulbs from each other. (h) Enlarged part showing irregularly distributed and aligned nm-sized Bi-S-Te mineral inclusions, and epoxy-filled crack. (i) Bulbous fossil with element distribution of N (j), O (k), and S (l), indicating an interior structure with possible former cell walls.

much smaller than the excitation volume of the electron beam, only mixed analyses with the organic material could be obtained (Table 2). Recalculation of the analyses without the organic compounds C, O, and N yielded an atomic ratio of Bi:(S,Te) near 1:1, indicating minerals such as ingodite Bi(S,Te) or joseite Bi₄(S,Te)₃. The example of the bulbous filament (Fig. 10g) with inclusions also shows a Bi(S,Te) mineral, located in the central part. The heterogenous BSE contrast is caused by different trace compounds of Fe and Cu. Element distribution of N and O (Fig., 10j, k) in a bulbous fossil, indicated by different BSE contrast (Fig. 10i), show an internal structure, possibly indicating a primary separation into different cells, whereas S (Fig. 10l) shows a systematic decrease towards the rims of the object, as a result of decay and/or fossilization.

Table 2 EDS analyses of Bi-sulfide-telluride inclusions

Analysis#	15 06 ¹	13 03 ²	13 ³ n=18	Min-max
S atom%	0.27	2.59	0.20	n.d. – 0.52
Te	0.13	0.06	0.12	n.d. – 0.51
Bi	0.29	2.05	0.24	0.01-0.68
Pb	0.03	n.d.	n.d.	
Fe	n.d.	0.19	n.d.	
Cu	n.d.	0.22	n.d.	
C	86.24	84.86	83.38	80.19-96.15
N	5.91	4.89	3.16	n.d.-7.18
O	7.13	5.14	10.12	2.74-15.78
Sum ⁴	100	100	100	
recalculated	15 06	13 03	13 n=19	Min-max
S atom%	38	51	37	3-55
Te	18	1	25	1-90
Bi	40	40	46	7-68
Pb	4	0		
Fe		4		
Cu		4		
Sum	100	100	100	

¹ Fig. 10h; ² Fig. 10f inclusion in channel; ³ average of 18 analyses, inclusions in matrix, Fig. 10b,c; ⁴ normalized; n.d. = not detected

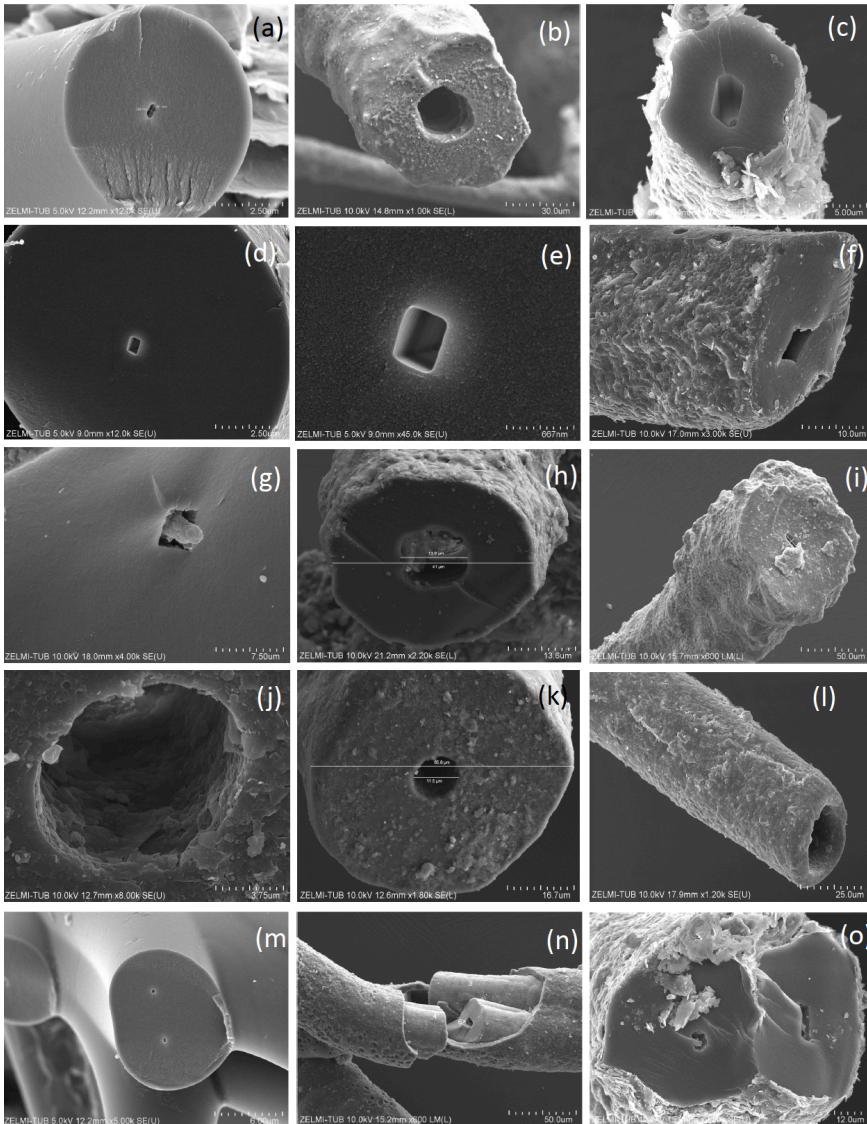


Fig. 11: SEM images of broken filamentous fossils, illustrating the central channel. (a,b,c) Six-sided channel in filament with (a) smooth outer surface, (b) dented surface, and (c) strongly mineralized surface. (d, e, f, g) Rectangular channel; (e) is enlarged part of (f). (h) Round, slightly irregular channel. (i) 4 µm x 6 µm wide channel on filament with dented surface. (j) Round channel, enlarged from (k), approximately 12 µm wide in a filament of nearly 70 µm diameter. (l) Slightly conical end of a filament with large, round channel. (m) Two filaments one with a small µm-wide channel attached to a hollow filament. (n) Channel in a filament with sheath-like structure. (o) Two filaments with six-sided channels.

A very characteristic feature of the filaments is a central channel (Fig. 11), observed in many but not all of the filaments. The cross section of the channel can be six-sided (Fig. 11a-c,m), rectangular (Fig. 11d-f), or round (Fig. 11h-l). The channel diameter is variable and ranges from approximately 0.5 μm to 25 μm in filaments with an outer diameter between approximately 5 μm and 100 μm ; examples in Fig. 11 show 5 μm with a channel of 260 nm x 550 nm (a), 50 μm with a channel of approximately 20 μm (b), 10 μm with a channel of 2.5 μm x 4 μm (c), 100 μm with a channel of 400 nm x 560 nm (d,e), 41 μm with a channel of 14 μm (i).

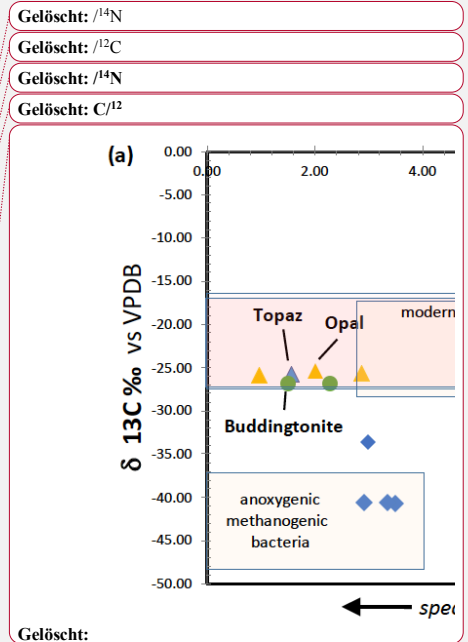
4.3 Stable isotopes and C/N variation

Stable isotopes of C and N were obtained from all bulk samples (Table 1); it was not possible to determine individual fossilized objects. In addition, we determined OM in black opal and OM adherent to topaz (see sample list in Franz et al., 2022a).

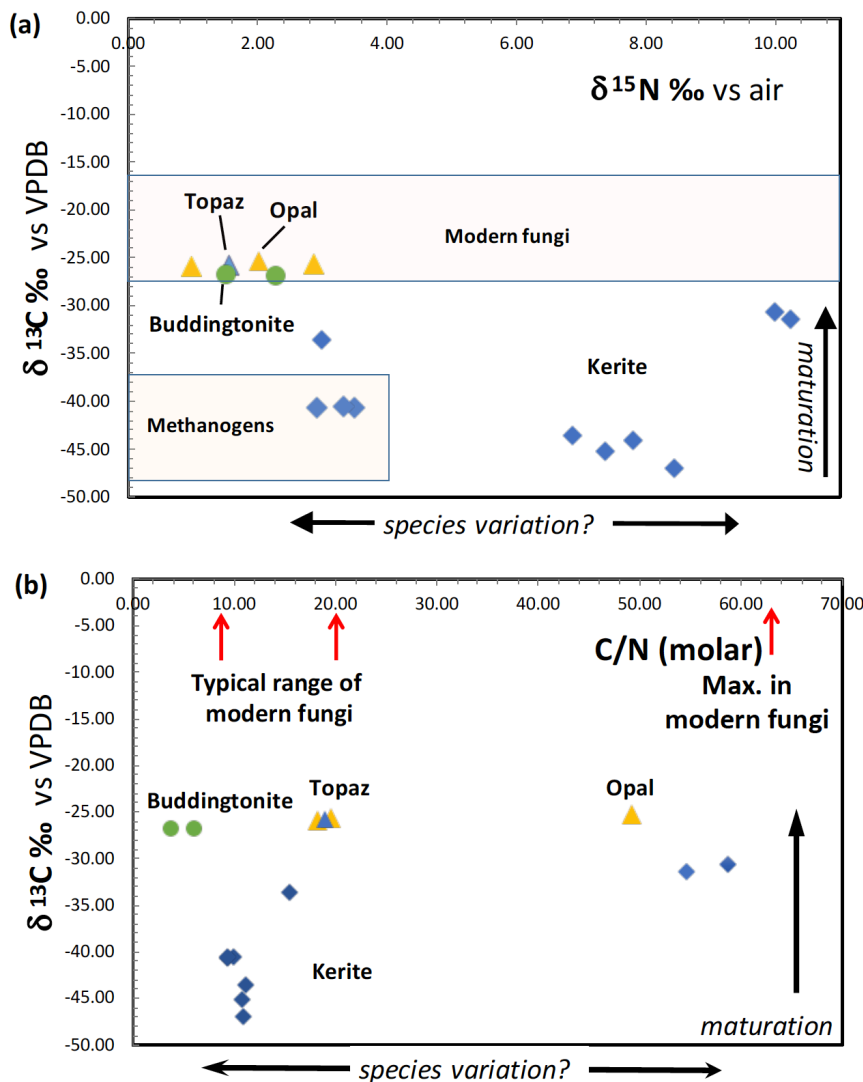
Results of $\delta^{13}\text{C}$ and $\delta^{15}\text{N}$ -determination and the molar C/N show a large variation (Fig. 12). All $\delta^{13}\text{C}$ values are negative, and for kerite fossils vary between -47 (sample 2) and -31 ‰ (sample 1); $\delta^{15}\text{N}$ values vary between ~3 to 4 ‰ (samples kerite 0, 4) and ~10 ‰ (samples 1, 3). OM associated with opal and topaz (considered as 'secondary') and buddingtonite, which obtained its N from decayed OM, is less negative and homogeneous in $\delta^{13}\text{C}$ with values between -25 and -27 ‰. The C-values should be considered as maximum values, since alteration either by deep-seated CO_2 from the mafic magmas or from meteoric waters would have increased $\delta^{13}\text{C}$. The close group of $\delta^{13}\text{C}$ and $\delta^{15}\text{N}$ values for secondary OM indicates that during maturation and decay they all have reached a similar value. The variation of the N-isotopes is not correlated with the C-isotopes, and there is also no correlation with C/N.

Table 3 Results of $\delta^{15}\text{N}$, $\delta^{13}\text{C}$, and molar C/N of bulk kerite samples

Sample#	weight mg	$\delta^{15}\text{N}$ ‰	mg N/sample	% N	$\delta^{13}\text{C}$ ‰	mg C/sample	% C	molar C/N
1	2.76	9.99	0.038	1.37	-30.66	1.91	69.07	58.74
2	2.37	8.44	0.067	2.85	-46.99	0.63	26.52	10.87
3	2.21	10.23	0.027	1.20	-31.38	1.24	56.10	54.58
4	2.52	2.98	0.033	1.31	-33.61	0.44	17.34	15.48
5	4.01	7.37	0.096	2.38	-45.19	0.88	21.98	10.78
6	3.14	7.79	0.037	1.19	-44.06	0.27	8.55	8.39
7	4.29	6.87	0.074	1.73	-43.58	0.71	16.54	11.17
Opal 8	50.15	2.02	0.013	0.03	-25.32	0.55	1.09	49.23
Topaz 9	54.46	1.56	0.023	0.04	-25.73	0.38	0.69	18.89



447



448

449

450

451

452

453

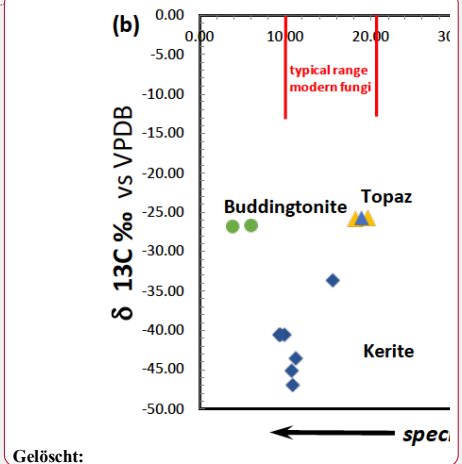
454

455

456

Fig. 12: (a) Results of determination of $\delta^{13}\text{C}$ and $\delta^{15}\text{N}$ of Volyn biota and degraded kerite. Symbols: Blue diamonds – dominantly filamentous kerite, with small amounts of flaky and spherical OM; yellow triangle - black opal with OM; blue triangle - OM adherent to topaz; green dots - buddingtonite from breccia (from Franz et al., 2017). Fields of modern fungi from Mayor et al. (2009) and methanogens are summarized in Struck (2012). (b) Molar C/N ratio of kerite fossils and degraded OM. Range of C/N of modern fungi from Mayor et al. (2009).

4.4 FTIR investigation



Gelöscht:

Gelöscht: ;

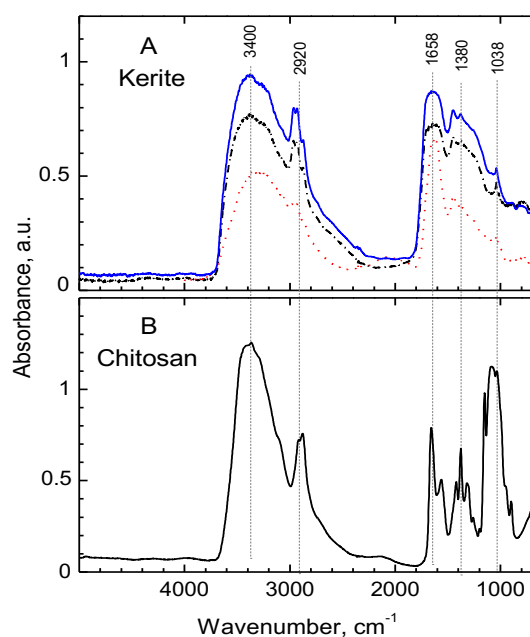
Gelöscht: modern marine sediments, phytoplankton and

Gelöscht: ic bacteria

Gelöscht: from Levin and Michener (2002), Peterson and Fry (1987), Rau et al. (1990, 1996), and

Formatiert: Durchgestrichen

463 All measured FTIR spectra of morphologically different kerite fragments in the sample #0 are
 464 very similar (Fig 13a) and resemble closely the chitosan spectrum (Fig 13b); both spectra are
 465 dominated by two main groups of absorption bands located in the regions of 3500-2500
 466 cm^{-1} and 1800-900 cm^{-1} . The first group consist of overlapping broad bands due to O-H and N-
 467 H stretching vibrations, with a group of characteristic narrow peaks of C-H stretching vibrations
 468 on their long-wavelength wing in the region of 2960-2870 cm^{-1} (Fig. 13; for detailed band
 469 assignments and for spectra of chitin see Table 1 Supplement). The peak in vicinity of 1650
 470 cm^{-1} is diagnostic of C=O group (Wanjun et al., 2005; Coates, 2011; Loron et al., 2019), the
 471 band at 1560 cm^{-1} (broad shoulder near 1570 cm^{-1} in kerite spectra) was assigned to N-H



472

473 **Fig. 13: FTIR spectra of filamentous fossil compared to standard materials chitin and**
 474 **chitosan. (a) Complete spectra of three pieces of sample kerite #0, the sample with less**
 475 **mineralization, showing two main regions of absorption: 3500 cm^{-1} to 2800 cm^{-1} and 1850**
 476 **cm^{-1} to 900 cm^{-1} ; (b) Standard material chitosan. Compared to chitosan the major**
 477 **absorption bands in kerite spectra are broader, the weak shoulder near 3100 cm^{-1} in**
 478 **chitosan spectrum is not present in kerite. The narrow triplet near 2950 cm^{-1} is observed**
 479 **as doublet in chitosan, shifted to lower wavenumbers. In the part from 1800 cm^{-1} to 700**
 480 **cm^{-1} , kerite shows only broad absorption, shifted towards higher wavenumbers compared**

to chitosan, with three superimposed distinct weak peaks at 1450 cm⁻¹, 1380 and 1038 cm⁻¹; the first is not present in chitosan, which has a number of distinct peaks in this region.

bending vibrations in amide group. The relatively weak band near 1420 cm⁻¹ (1450 cm⁻¹ in kerite) was attributed to C-H bend (Loron et al., 2019), and the sharp peak at 1380 cm⁻¹, which was reported in cellulose, chitosan, and chitin spectra, was assigned to superposition of O-H bend (pyranose ring; Li et al., 2009) and symmetrical bend of CH₃ group. A band centered near 1315 cm⁻¹ in chitin and chitosan spectra due to C-N stretching vibrations in amide group (Vasilev et al., 2019; Wanjun et al., 2005) is not observed in kerite.

A broad, weak band at around 2100 cm⁻¹ is present in spectra of kerite and chitosan (Fig. 13), and the same type of weak bands are shown in published chitosan spectra (see Table 1 Supplement), but not mentioned and assigned. It can probably be attributed to overtone or combination bands of pyranose ring vibrations. At lower wavenumbers, in all measured spectra there is a series of strong (1150, 1180, 1030 cm⁻¹) and several weak bands caused by different types of C-O vibrations in polysaccharides (Nakamoto, 1997; Wanjun et al., 2005; Li et al., 2009; Coates, 2011; Loron et al., 2019; Vasilev et al., 2019).

A general observation is that in kerite spectra, compared to chitosan, all characteristic absorption bands of the amide group and the pyranose ring become broader and weaker, in agreement with earlier studies of spectroscopic changes during chitin/chitosan degradation (Wanjun et al., 2005; Zawadzki and Kaczmarek; 2010; Vasilev et al., 2019). Nevertheless, the main absorption features caused by amide group, diagnostic of chitosan, are still present in kerite spectra.

5 Discussion

5.1 Interpretation of morphological and internal characteristics

The Volyn biota show an astonishingly large variation of different types of filaments and other forms, pointing to the interpretation that different organisms were involved. We have already interpreted the flaky objects of OM on the surface of beryl crystals (Fig. 2e,f) as biofilms (Franz et al., 2022a). Agglutinated filaments (Fig. 6f) and the hollow object agglutinated to a filament (Fig. 7i) can similarly be interpreted as fossilized biofilms. The sheath-structure (obvious e.g. in Fig. 5i, j) is also an indication for the presence of a biofilm or extracellular polymeric substances (EPS).

Gelösch: 5.1 Model for a Precambrian deep biosphere ecosystem

The Volyn occurrence is a well-preserved example of a fossil ecosystem of the deep biosphere. We exclude an a-biotic origin as previously postulated (Ginzburg et al., 1987; Lu'kyanova et al., 1992) because of the extremely low $\delta^{13}\text{C}$ values and the large variation in morphology. In combination with textural arguments, the age determination of muscovite, formed in pseudomorphs after beryl, point to a minimum age of 1.5 Ga (Franz et al., 2022b); the maximum age is restricted by the intrusion of the igneous rocks at 1.760 Ga (Shumlyanskyy et al., 2021).

The geological context argues for a continental, terrestrial environment, because the KPC intruded into continental crust most likely in a within-plate tectonic setting (Shumlyanskyy et al., 2012, 2017). After intrusion uplift to the erosion level occurred, documented by an unconformity, and sedimentation started with sandstones and shales at approximately 1.4 Ga (Zbranki Formation; Gorokov et al., 1981), later than or coeval with the pseudomorph formation and the minimum age of the microfossils. The depth, where the organisms lived, is an open question, but the occurrence in the underground mines indicate a depth of up to at least 150 m. The age of 1.5 Ga is much later than the oxygenation of the Earth's atmosphere allowing the evolution of complex species and ecosystems on the land (sub)surface.

The Precambrian age clearly argues for fossils of microorganisms. The large size of the filaments up to cm in length is atypical for bacteria and archaea. However, Volland et al. (2022) described recent cm-long bacteria, and the term 'microorganisms' in the original description that they can be observed only on the microscopic scale, is not really appropriate. Putative cm-sized Precambrian fossils (different from the Volyn biota) were reported from the 2.1 Ga old Francevillian biota (El Albani et al., 2014); however, they are completely pyritized and occur in diagenetically overprinted black shales, which makes the interpretation difficult.

Gelösch: 2

Gelösch: Summary and i

Gelösch: species

552 Some objects have a base onto which they grew (Figs. 3j-l, 8, 9a-c) and one object shows a
553 hollow lower part, from which bulbous outgrowths originate (Fig. 7a, b), pointing to sessile
554 organisms. Filaments are generally fragmented, but a few filaments have been found with two
555 intact ends (Figs. 4c, g, 6i, o), and we interpret this as non-sessile, planktonic organisms, or
556 organisms which grew in a soft (possibly organic or clay mineral) substrate.

Gelöscht: either floating

Gelöscht: or as an indication for growth of organisms

557 Thickness of the filaments varies from $\leq 10 \mu\text{m}$ to $>200 \mu\text{m}$. In filaments with diameter up to
558 approximately $30 \mu\text{m}$, branching with thinning out of the branch clearly show that these are
559 within-species variations (irregular diameters of filaments, Fig. 2i, j, are interpreted as collapse
560 structures during fossilization). However, very thick filaments with diameters in the range of
561 $\geq 200 \mu\text{m}$ with a structured, bulbous surface (e.g. Fig. 6), or conical objects (Fig. 4m) are
562 interpreted as different species. The length of both types of filaments reaches the mm-range,
563 and since they are fragments possibly up to cm-length.

564 Branching as indication for growth of the organisms is typical in the thin filaments, with Y-,
565 T-, double-T-, and multiple branching (Fig. 3), but anastomosing was not observed. In thick
566 filaments with diameter near $200 \mu\text{m}$ branching was not found. The ends of filaments also hint
567 to the type of growth. Simple round ends are rare, more typical are ball-shaped ends (Fig. 4).
568 Ball-shaped outgrowths along filaments are interpreted as beginning of a branching (Fig. 4h).
569 In the complete filaments (Fig. 4c, g) with one end thinning out, one with a ball-shaped end,
570 the thinning-out end is possibly the origin, the ball-shaped protrusions the growing end, because
571 ball-shaped ends are rather continuous in shape, from a small protrusion (Fig. 4b) to a more
572 complete ball (Fig. 4f, i). Similar protrusions were found at the end of recent, large bacterial
573 filaments (Volland et al., 2022). However, branched, thinning-out ends of the filaments (Fig.
574 3j-l, m) indicate ends similar to spitzenkörper, what in modern fungi is described as a
575 continuous and indefinite process of cell extension (Fischer et al., 2008).

576 Segmentation in thin filaments (Figs. 5m, 6g, h) with distances of a few μm up to tens of μm is
577 accentuated by mineralization (Fig. 5n), with irregular ridges caused by mineralization. Thick
578 filaments do not show a clear segmentation; the morphology is more irregular and shows
579 rounded, polygonal structures on the surface with dimensions of approximately $20\text{-}30 \mu\text{m}$
580 (parallel to filament axis) x $35\text{-}70 \mu\text{m}$ (perpendicular to filament axis) (Figs. 5g, h, i, 6b, c).
581 Between the polygonal structures on the surface, remnants of a sheath are visible. In cross
582 section (Fig. 10) segmentation is clearly visible by cracks with a distance of approximately 50-
583 $100 \mu\text{m}$.

586 Bulbous forms (Figs. 7a, b, 8) mark the beginning of growth of some objects, and bulbous
587 outgrowths are very typical for thick filaments (Fig. 6, d, f), which extend into approximately
588 20 μm large objects, which consist of smaller bulbs (Fig. 6l, n). In thin filaments with typical
589 branching, the outgrowths are rare and more regularly ball-shaped (Figs. 3f, g, 4h), indicating
590 one species with prominent growth by branching of thin filaments, and another species with
591 growth by outgrowths along thick filaments.

592 Among the spherical objects, only the small ones with a size of a few μm (Fig. 9l-o) resemble
593 spores or other types of seeds/fruit bodies. The irregular, large objects several hundred μm in
594 size (Fig. 9d-k) do not fit into any scheme of known (micro)organisms. Similarly, there is no
595 obvious interpretation for the large bowl-shaped and irregular hollow objects (Fig. 8). The small
596 double-object with a partly preserved sheath (Fig. 9a-c) grown on a substrate has some
597 similarities with cell division.

598 The function of the conspicuous central channel (Fig. 11) in many, but not all filaments with
599 different shape in cross section is speculative, likely providing pathways for transport of
600 components for cell extension along the filament axis. In one example we observed a type of
601 filling in the channel (Fig. 11g), so in the original organisms it might have been filled with an
602 easily degradable substance. It is not clear if a hollow form (Fig. 7e, l) is a different phenomenon
603 or due to special preservation conditions. The width of the preserved rim is in the same order
604 of magnitude as the silicified rim (1-2 μm) and therefore it might just be a remnant of a filament,
605 in which the central part was completely degraded.

606 Another special feature of the internal structure are the nanometer-sized mineral inclusions of
607 Bi-S-Te minerals (Fig. 7). The organisms were able to concentrate these elements, either
608 irregularly distributed (Fig. 7c) or rod-like aligned (in a bulbous object; Fig. 7h) **or within the**
609 **channel (Fig. 7e)**. It is unclear if the relatively large Bi-S mineral with some Cu and Fe contents
610 in the center of a thick filament, in the central channel is the original position of the Bi-S
611 concentration or an effect of fossilization. Modern fungi are able to concentrate Te (and Se) as
612 nm-sized crystals (Liang et al., 2020) and could be used in technology for soil mycoremediation
613 (Liang et al., 2019). In black shales, the organophilic element Bi might behave similar as Se
614 (Budyak and Brukhanova, 2012). Biogeochemistry of Te is probably analogous to Se (Missen
615 et al., 2020), but little is known about the link of Bi to S and Te in OM (such as in coal, e.g.
616 Finkelman et al., 2019). The concentration of Bi-S-Te in the organisms of the Volyn biota is
617 another indication for fungi-like organisms, although other organisms are also able to
618 concentrate Te (Missen et al., 2020).

Gelöscht: (Fig. 7e)

Remnants of cell membranes, separating individual cells, could not be identified, and to answer the question if some of the organisms were multicellular is speculative. However, the large size of many objects of the Volyn biota already indicates that possibly they were not single-celled but multicellular, notwithstanding that single-cell bacteria (*Thiomargarita magnifica*; Volland et al., 2022) can reach the size of cm. These macroscopic single-cell bacteria show a very simple straight filament, whereas the large objects from the Volyn biota show a much more complicated form; the surface of large filaments shows a bulbous structure with sizes in the order of tens of μm (Figs. 5g-i, 6c, f, 9a, b), well visible with a polygonal network (Fig. 5j). In the internal structure we also see phenomena that could be explained as separate cells, such as the gaps in a filament (Fig. 10a) or in a bulbous object (Fig. 10g). The interior structure visible in the element distribution of N (Fig. 7j) might indicate the original distribution in former interior cell walls, in which chitin-like substance was concentrated. Finally, the small spherical object shown in Fig. 9a, b might be taken as two cells, with an envelope of a sheath.

Gelöscht: ¶

5.2. Stable isotopes

Gelöscht: 3

Modern fungi show a very wide variation of $\delta^{15}\text{N}$ from -5 ‰ to +25 ‰, with the main cluster between -5 ‰ and +12 ‰, and $\delta^{13}\text{C}$ is restricted to -19 ‰ to -29 ‰ $\delta^{13}\text{C}$, with the main cluster at -22 ‰ to -28 ‰ $\delta^{13}\text{C}$ (Mayor et al., 2009; Fig. 12a). Whereas the N-isotopic signature of kerite is consistent with the interpretation as fossil fungi, the C-isotopic signature is much lower than that of modern fungi. However, fungi live from consumption of organic matter, and the C-isotopic signature is then transferred to the fungi without strong isotopic effect (Peterson and Fry, 1987). I. e. during incorporation of carbon from modern plants to fungi, the $\delta^{13}\text{C}$ -signature of -27 ‰ to -30 ‰ in plants changes to -25 ‰ to -27.5 ‰ $\delta^{13}\text{C}$ in fungi (e.g. Högberg et al., 1999). Assuming that the isotope fractionation in the Volyn biota was similar, the consumed organism had a C-isotopic signature of c. -35 ‰ to -50 ‰ $\delta^{13}\text{C}$. These very low values are consistent with the interpretation that the primary organisms were methanogens. Another factor, which must be considered, is intracellular heterogeneity as observed in bacteria (Lepot et al., 2013). The membrane (lipids) can have a signature of 10 ‰ $\delta^{13}\text{C}$ lower than the bulk cell, and degradation during fossilization of the proteins and polysaccharides can lower the now determined C-signature. It is also possible that the fungi consumed biofilm. Fossil biofilms of the 2.75 Ga Hardey Formation (Australia), probably coexisting with methanogens, methanotrophs, and sulfur-metabolizing bacteria have $\delta^{13}\text{C}$ of -55 ‰ to -43 ‰ (Rasmussen et al., 2009), well in the range of $\delta^{13}\text{C}$ -values observed here. The biofilms, described by

Gelöscht: However, fungi live from consumption of organic matter, and this C-signature is transferred to the fungi. During consumption of C

Gelöscht: anoxygenic/

Gelöscht: ic bacteria

660 Rasmussen et al. (2009), lived in syngedimentary cavities similar to stromatolites, pointing to
661 the importance of cavities for the preservation of organic matter, similarly as the biofilms at
662 Volyn in the deep biosphere.

663 Maturation clearly affects the C- and N-isotope ratios, which we see in degraded OM preserved
664 in black opal, in OM adherent to topaz, and buddingtonite which obtained its NH_4 from OM.
665 These samples have much more positive $\delta^{13}\text{C}$ values around -26 ‰ and more homogeneous
666 $\delta^{15}\text{N}$ values near +1.5 to +3 ‰ (Fig. 12a). In contrast, the large variation of $\delta^{15}\text{N}$ between 3 ‰
667 and 10 ‰ in the kerite samples (Fig. 12a) and C/N between 10 and >50 (Fig. 12b) possibly
668 indicates a variation of the species. These values were less influenced by maturation, as there
669 is no correlation between $\delta^{13}\text{C}$ and C/N in all samples (fossils and degraded OM). Alleen et al.
670 (2018) in their description of the 3.4 Ga old Strelley Pool microfossils (Western Australia)
671 argued that though the fossils experienced heating up to 300 °C, the C/N did not change
672 significantly. Also, for anthracite coal it has been shown that the original C/N did not vary with
673 coalification (Anwita et al., 2020).

674 Loron et al. (2019) reported fossil fungi from the 1 Ga Grassy Bay Fm Canada, and provided
675 proof via chitin remnants (FTIR) and showing the characteristic bilayered fungal cell walls
676 (TEM data). However, the few SEM images for the Grassy Bay biota do not allow a comparison
677 with the Volyn biota. Following their discussion, the FTIR investigation of the filamentous
678 Volyn sample shows good indications for preserved chitosan as part of the OM. Degradation
679 studies of chitosan (Wanjun et al., 2005; Zawadzki and Kaczmarek; 2010; Vasilev et al., 2019)
680 showed that the spectra of kerite has the same characteristic bands as chitosan at approximately
681 250 °C; at lower as well as at higher temperatures these bands disappear. Completely
682 independent temperature estimates for the fossilization based on phase equilibria of Be minerals
683 yielded the same temperature range (Franz et al., 2017).

684 **5.3 Taxonomy and comparison with Precambrian biota**

685 Film-like microfossils were described from the 3.4 Ga old Strelley Pool (Western Australia;
686 Alleen et al., 2018), the 3.3-3.5 Ga old Onverwacht Group (Australia; Westall et al., 2001),
687 from the 2.75 Ga old Hardey Formation (Australia; Rasmussen et al., 2009) and there is little
688 doubt that biofilms existed for a long time in the Earth's history and are an integral component
689 of the ancient life cycle (Hall-Stoodley et al., 2004). It seems safe to assume that the irregular
690 (Fig. 2f, and images in Franz et al., 2022a) and sheath-like structures (Figs. 5i,j, 6f, 9a) of the
691 Volyn biota were biofilms.

Gelöscht: fossil

Gelöscht: 4

694 We have already pointed out that some of the organisms show analogies to fungi. Based on the
 695 molecular clock technique, Wang et al. (1999) estimated the divergence between the three-way
 696 split of the animal-plant-fungi **kingdoms** at 1.58±9 Ma, much earlier than the ‘Precambrian
 697 explosion’. This age is in the same range as the minimum age of the Volyn biota. Other
 698 molecular clock estimates indicate that the first zygomycetous fungi occurred on Earth during
 699 the Precambrian, approximately 1.2–1.4 Ga ago (review in Krings et al., 2013). Diversification
 700 of fungi and transition to land was dated at ca. 720 Ma (Lutzoni et al., 2018) and they estimate
 701 the origin of fungi at ca. 1240 Ma, similarly as Berbee et al. (2020), who placed the origin of
 702 fungi at ca. 1300 Ma. If indeed the Volyn biota contain fungi-like organisms, their origin as
 703 well as colonization of land occurred earlier than ca. 1500 Ma.

704 Bengtson et al. (2017) reported fungus-like organisms **in the 2.4 Ga Ongeluk Formation (South**
 705 **Africa)** from the deep biosphere, which are, however not terrestrial but marine. The important
 706 fact is that these fossils were found also in open cavities, though of a completely different size,
 707 mm-amygdales in low-grade metamorphic basalt, in contrast to the huge cavities of tens of
 708 meter size in the pegmatites from Volyn. The filaments from the Ongeluk biota with a diameter
 709 of ca. 2 µm to 12 µm are generally thinner than the Volyn biota and show anastomosis, but also
 710 Y- and T-branching, and sometimes bulbous protrusions, 5-10 µm in diameter. A special feature
 711 is what Bengtson et al. (2017) call ‘broom structure’, diverging filaments growing from a
 712 substrate of clay minerals (chlorite), and the filaments consist also of the same type of chlorite.
 713 These structures (shown in 2D in thin sections) could be similar as the object from the Volyn
 714 biota (Fig. 3j, k, l), and what we called ‘multiple branching’ (Fig. 3c, e, g). A significant
 715 difference between the two biota is the fossilization process, which resulted in the Ongeluk
 716 biota in complete replacement of the filaments by clay minerals, whereas at Volyn fossilization
 717 is restricted to the outermost rim and most of the C is preserved (Franz et al., 2022a).

718 Good evidence for fungi-like organisms were reported from the early Ediacaran Doushantuo
 719 biota, at approximately 635 Ma (Gan et al., 2021). These fossils are pyritized, but with remnants
 720 of organic matter, and consist of branching filaments (Y-, T-branching, but also with A- and H-
 721 type and anastomosis) and associated hollow spheres. Compared to the Volyn biota, the
 722 filaments are thinner (two types, one with average 6.8 µm, one with average 2.7 µm), whereas
 723 the observable length in thin section with hundreds of µm is possibly in the same range as in
 724 the Volyn biota. The spheres of the Doushantuo biota are hollow and coaxially aligned, but also
 725 similar to what we described as ball-shaped outgrowths; their size varies from average 16 µm
 726 to 20 µm in small ones and large spheres with 36 µm to 102 µm, similarly to the Volyn biota
 727 (Fig. 4h, i for the small spheres, Fig. 4j for large spheres). The fact that the spheres of the

Gelöscht: kingdoms

Gelöscht: s

Gelöscht: s

Gelöscht: from the 2.4 Ga Ongeluk Formation (South Africa),

733 Doushantuo Formation are hollow is possibly due to the fact that they are mostly pyritized, i.e.
734 most of the organic matter was decomposed. The small spheres were interpreted (Gan et al.,
735 2021) as possible spores, the larger ones were possibly symbiotic organisms living together
736 with the fungi.

737 Myxomycetes (slime molds) are other possible eukaryotes, which might have existed in the
738 Proterozoic, although Stephenson et al. (2008) considered 50 My as the oldest fossil record.
739 Their diverse morphology during the different stages of their life cycle including amoeboid
740 forms leaves much room for speculation. Filamentous, mm-long sporocaps, such as shown in
741 Fig. 3a in Rikkinen et al. (2019) are similar to what we see in Fig. 4b. The structured surfaces
742 shown in Fig. 6 are somehow similar to what Dagamac et al. (2017) showed in their Figs. 7-9
743 from recent *Arcyria complex*, though on the μm -scale, whereas those from the Volyn biota are
744 much larger. The image of multiple, conical filaments with claw-like ends, growing from a
745 common center (Fig. 3j, k, l) is similar to *Copromyxa protea* shown by Schnittler et al. (2012)
746 in their Fig. 4-2. Hollow objects (Fig. 7, i-k, m, n) resemble open sporocaps of Liceaceae
747 (Schnittler et al., 2012, in their Fig. 5-12). Finally, large objects such as the open, bowl-shaped
748 one with bulbous outgrowths (Fig. 8) could be interpreted as plasmodium of a myxomycete
749 with beginning development of fruiting bodies (e. g. Fig. 2, life cycle of myxomycetes,
750 transition from stage H1 to A; Stephenson and Schnittler, 2016).

751 Other possible organisms described from the Precambrian are all very different from the Volyn
752 biota and are excluded as possible analogues e.g. palynomorphs, which are among the earliest
753 clear records of terrestrial life (Wellman and Strother, 2015); the 1.67 Ga eukaryotic
754 Changcheng biota (Miao et al., 2019), or vase-shaped metazoan microfossils, considered as the
755 oldest evidence for heterotrophic protists, e.g. Urucum Formation, Brazil (Moraes et al., 2017).

756 Most of the Precambrian biota listed in the literature are considered as photosynthetic
757 organisms, probably not a likely analog for the Volyn biota. E. g. the 770 Ma (Cryogenian)
758 Chichkan Fm. in Maly Karatau, Kazakhstan (Sergeev and Schopf, 2010) contains biota in
759 fine-grained black chert, which were deposited in a mid-shelf and a near-shore environment
760 with stromatolites. Most of the biota listed by Sergeev and Schopf (2010) are cyanobacteria,
761 rather small mostly up to the 10 μm range and thus do not serve as analogues for the Volyn
762 biota. They also list a number of larger protista (*incertae sedis*) in the 100 μm -range, however
763 with little morphological similarity to the Volyn biota. No similarity was found to eukaryotes
764 (acritarchs) from 1.1 Ga old Taoudeni basin, Mauretania (Beghin et al., 2017). Red algae

Formatiert: Schriftart: Kursiv

Formatiert: Schriftart: Nicht Fett

Formatiert: Schriftart: Kursiv

Gelöscht: (

Gelöscht:)

Gelöscht: ,

Gelöscht: described from the ca. 1.08 Ga old Nunsuch Shale of the Oronto Group (Michigan). This microbiota shows cell clusters, with little similarity to morphologies of the Volyn biota. However, the Nunsuch biota come from a surface environment, whereas the Volyn biota from the deep biosphere. We do not see similarity with

Gelöscht: (

Gelöscht:)

Gelöscht: with

Gelöscht: (

Gelöscht: ;

(rhodophytae) from the 1.05 Ga Hunting Fm, considered as among the oldest eukaryotes (Butterfield, 2000; Gibson et al., 2018) are photosynthetic organisms and can also be excluded.

5.4 Model for a Precambrian deep biosphere ecosystem

The Volyn occurrence is a well-preserved example of a fossil ecosystem of the deep continental biosphere. We exclude an a-biotic origin as previously postulated (Ginzburg et al., 1987; Lu'kyanova et al., 1992) because of the extremely low $\delta^{13}\text{C}$ values and the large variation in morphology. A-biotic pseudofossils have been produced experimentally, e.g. by Nims et al. (2021) and references therein, when sulfide is oxidized in the presence of organics. These 'organic biomorphs' show a large variety of morphologies, mostly filamentous, but also globular. In a siliceous environment (for many cases chert) such organic biomorphs can be replaced by silica, and their morphology can be well preserved. However, for the Volyn biota such a sulfide rich environment did not exist. Additionally, we take the presence of chitosan as another indication for a true fossil. McMahon (2019) provided another example of pseudofossils, which is however restricted to an iron-rich environment; these pseudofossils consist of hematite or Fe-oxides/hydroxides, conditions not realized in the highly differentiated pegmatites, which are very poor in Fe. Rouillard et al. (2018) produced another type of pseudofossils with an amazing large variety of morphologies, which might occur in hydrothermal, silica-rich rocks, but requires a high activity of Ba, for which there is no indication in the Volyn pegmatites.

In combination with textural arguments, the age determination of muscovite, formed in pseudomorphs after beryl, points to a minimum age of 1.5 Ga (Franz et al., 2022b); the maximum age is restricted by the intrusion of the igneous rocks at 1.760 Ga (Shumlyanskyy et al., 2021).

The geological context argues for a continental, terrestrial environment, because the KPC intruded into continental crust most likely in a within-plate tectonic setting (Shumlyanskyy et al., 2012, 2017). After intrusion uplift to the erosion level occurred, documented by an unconformity, and sedimentation started with sandstones and shales at approximately 1.4 Ga (Zbranki Formation; Gorokov et al., 1981), later than or coeval with the pseudomorph formation and the minimum age of the microfossils. The depth, where the organisms lived, is an open question, but the occurrence in the underground mines indicate a depth of up to at least 150 m. The age of 1.5 Ga is much later than the Great Oxidation Event of the Earth's atmosphere, allowing for the evolution of complex species and ecosystems on the land (sub)surface. The supply of organic matter to the underground for the production of the high

amounts of kerite is speculative. In a geyser system, which we invoke for the whole geological situation, intense growth of organisms at the surface is a common observation. In such systems continuous exchange between surface and depth is evident. This also excludes very deep (more than several hundreds of meters) biosphere, more likely near to the surface. Unfortunately, no information is available right now, which of the many pegmatites from the Volyn pegmatite field contains kerite and which – in what depth – are devoid of kerite. This remains to be investigated in the future.

Drake et al. (2017) reported partly mineralized fungi from the deep continental (granitic) biosphere (up to 740 m). The fossilization process also included maturation of the OM and final mineralization by clay minerals. The source of carbohydrates was living or dead bacterial biofilms, similar to what we speculate about the Volyn biota.

The large size of the filaments up to cm in length is atypical for bacteria and archaea. Although Volland et al. (2022) described recent cm-long bacteria, these are still the exception, and it is more likely that some of the Volyn biota were multi-cellular eukaryotes. Their suggested age of 1.5 Ga is the age range given for the first appearance of eukaryotes (see review in Butterfield, 2015). Putative cm-sized Precambrian fossils (different from the Volyn biota) were reported from the 2.1 Ga old Francevillian biota (El Albani et al., 2014); however, they are completely pyritized and occur in diagenetically overprinted black shales, which makes the interpretation difficult.

6 Summary and conclusions

The exceptional 3D preservation of the 1.5 Ga Volyn biota is due to the fossilization conditions in open cavities, with SiF₄-rich fluids as the driving agent. There are a number of indications that fungi-like organisms were likely an important part of the microecosystem – hyphen with branching (though not anastomosing), growth in thinning-out ends, and also in bulbous extrusion, both at the end of filaments and along the filaments. Sheath-like structures are clearly visible, and there are good indications for a former biofilm and extracellular proteinic substance. The large size and internal structure of the organisms and the segmentation visible on thick filaments points to multicellular organisms, and the nano-sized inclusions of Bi(S,Te) crystals have an astonishingly good analog in recent fungi. Other organisms, which might have been present in this subsurface micro-ecosystem are myxomycetes or myxomycete-like. The stable N- and C-isotopic signature is in accordance with such an interpretation.

844 The fungi-like organisms possibly lived from lithotrophic methanogens; alternatively or
845 additionally bacteria such as cyanobacteria were transported from the surface downwards into
846 the cavities. The geyser system of the Korosten Pluton provided an ideal framework for growth
847 of bacterial or algal organisms at the surface. In the deep biosphere, benthic forms of the
848 organisms are observed as well as organisms floating in water or growing in soft clay media,
849 but not attached to the clay.

850 The Volyn biota show that fungi-like organisms developed before 1 Ga (Loron et al., 2019),
851 and support the speculation that the fossils from the 2.4 Ga Ongeluk Formation were fungi-like
852 organisms (Bengtson et al., 2017). Molecular clock data, especially the three-way split of the
853 kingdoms animals-plants-fungi at 1.58±9 Ma (Wang et al., 1999) are still uncertain, but our
854 data indicate that it must have occurred early in the Proterozoic.

855 The Volyn biota also prove that a deep continental biosphere was already present in the Early
856 Mesoproterozoic/Late Paleoproterozoic. It is known that in the subseafloor environment
857 microbial life existed in the Archean (Cavalazzi et al., 2021), as described from the 3.4 Ga old
858 Onverwacht Group of the Barberton greenstone belt, but from the continental environment this
859 has not yet been reported. Furthermore, the Volyn biota must have been highly radiation
860 resistant (e.g. the bacteria *Deinococcus radiodurans* or *Thermococcus gammatolerans*; see
861 review in Matusiak, 2019), because a U-Th-K-rich granitic-pegmatitic system has a high
862 radiation level. During the mining operations in Soviet times, a high Rn content was measured
863 inside cavities, when they were broken into. The general radiation levels, 3000 times higher
864 than the allowed limit at that time, were even higher 1.5 billion years ago. Deeply black-colored
865 quartz crystals in the pegmatites are of the 'morion' type and also indicate high radiation.
866 Recent observations at the Tschernobyl power plant have led to the speculation about
867 radiotrophic fungi (e.g. Matusiak, 2019; Prothmann and Zauner, 2014), which produce melanin
868 as a protection against radiation and enhancement of fungal growth via capture of ionizing
869 radiation for energy conversion (Dadachova et al., 2007; Tugay et al., 2017). Mycoremediation
870 is at least a well-documented mechanism for a very effective method of radio nuclides pollutant
871 removal considering the versatility of fungi in terms of their ecology, nutritional modes,
872 adaptability, morphology, physiology, and metabolism (Shourie and Vijayalakshmi, 2022).
873 Fungi are known as extremophylic organisms (e.g. Blachowicz et al., 2019) and we can expect
874 that in the Proterozoic or possibly already earlier in Earth history similar organisms were active
875 and resistant to a high radiation level, in an epoch when the ozone layer was not yet fully
876 developed.

Gelöscht: ic bacteria

878

879

880 Acknowledgements

881 We thank three anonymous reviewers for their helpful and constructive suggestions, Tina
882 Treude for editorial handling, Martin Schnittler for discussion and literature about
883 myxomycetes, and Felix Haesler for discussion about fungi.

884

885 Funding

886 Alexander von Humboldt foundation provided support for VK during his stay in Berlin in 2022.

887

888 Author contribution

889 Concept, writing, interpretation, EMPA and SEM data acquisition - GF; IR spectra, writing -
890 VK; sampling - VC, PL; stable isotopes - US; SEM - UG; EMPA - JN.

891

892 References

893 Alleon, J., Bernard, S., Le Guillou, C., Beyssac, O., Sugitani, K., and Robert, F.; Chemical
894 nature of the 3.4 Ga Strelley Pool microfossils, *Geochem. Persp. Lett.*, 7, 37-42, 2018. doi
895 107185/geochemlet.1817.
896 Anwita, Gosh, S., Varma A. K., Das, S. K., Pal, D., and Solanki, G () Metamorphic
897 transformations of nitrogen functionalities: Stabilization of organic nitrogen in anthracite and its
898 effect on $\delta^{15}\text{N}$ parameter, *Marine Petrol. Geol.*, 112, 2020,
899 doi.org/10.1016/j.marpetgeo.2019.104090.
900 Beghin, J., Storme, J.-Y., Blanpied, C., Gueneli, N., Brocks, J. J., Poulton, S. W., and Javaux,
901 E. J.: Microfossils from the late Mesoproterozoic – early Neoproterozoic Atar/El Mreiti Group,
902 Taudeni basin, Mauretania, northwestern Africa, *Prec. Res.* 291, 63-82, 2017.
903 Bengtson, S., Rasmussen, B., Ivarsson, M., Muhling, J., Broman, C., Marone, F., Stampanomi,
904 M., and Bekker, A.: Fungus-like mycelial fossils in 2.4 billion-year-old vesicular basalt, *Nature*
905 *Ecol. Evol.*, 1(6), 1-6, 2017.
906 Berbee, M. L., Strullu-Derrien, C., Delaux, P.-M., Strother, P. K., Kenrick, P., Selosse, M.-A.,
907 and Taylor, J. W.: Genomic and fossil windows into the secret lives of the most ancient fungi,
908 *Nature Rev. Microbiol.*, 18, 717–730, 2020.
909 Blachowicz, A, Chiang, A. J., Elsaesser, A., Kalkum, M., Ehrenfreund, P., Totok, T., Wang, C.
910 C. C., and Venkateswaran, K.: Protemoic and mteabolic characteristics of extremophilic fungi
911 under simulated Mars conditions, *Front. Microbiol.* 10:1013, 2019, doi:
912 10.3389/fmicb.2019.01013
913 Budyak, A. E., and Brukhanova, N. N.: Selenium, bismuth, and mercury in black shale-hosted
914 gold deposits of different genetic types, *Geochem. Int.*, 50, 791-797, 2012.
915 Butterfield, N. J.: *Bangiomorpha pubescens* n. Gen., n. sp.: Implications for the evolution of
916 sec, multicellularity, and the Mesoproterozoic/Neoproterozoic radiation of the eukaryotes,
917 *Paleobiol.*, 26, 386-404, 2000.
918 Butterfield, N. J.: Early evolution of the eukarya, *Palaeontology*, 58, 5-17, 2015. doi:
919 10.1111/pala.12139
920 Cavalazzi, B., Lemelle, L., Siminovic, A., Cady, S. L., Russell, M. J., Bailo, E., Canteri, R.,

Gelöscht: Reviewers

Feldfunktion geändert

Enrico, E., Manceau, A., Maris, A., Salomé, M., Thomassot, E., Bouden, N., Tucoulou, R., and Hofman, A.: Cellular remains in a ~3.42-billion-year-old subseafloor hydrothermal environment, *Sci. Adv.*, 7, eabf3963, 2021.
 Coates J.: Interpretation of infrared spectra, a practical approach, *Encyclopedia of Analytical Chemistry* R.A. Meyers (Ed.), copyright John Wiley & Sons Ltd., 2011.
 Dadachova, E., Bryan, R. A., Huang, X., Moadel, T., Schweitzer, A. D., Aisen, P., Nosanchuck, J. D., and Casadevall, A.: Ionization radiation changes the electronic properties of melanin and enhances the growth of melanized fungi, *PLoS ONE*, 5, 1-13, 2007.
 Dagamac, N. H., Dela Cruz, T. E., Rea-Maninta, M. A. D., Aril-Dela Cruz, J. V., and Schnittler, M.: Rapid assessment of myxomycete diversity in the Bicol Peninsula, Phillipines, *Nova Hedwigia*, 104, 1-3, 31-46, 2017.
 El Albani, A., Bengtson, S., Canfield, D. E., Riboulleau, Bard, C. R., et al.: The 2.1 Ga old Francevillian biota: Biogenecity, taphonomy and biodiversity, *PLoS ONE* 9(6): e99438, 2014. doi: 10.1371/journal.pone.0099438.
 Finkelman, R. B., Dai, S., and French, D.: The importance of minerals in coal as the hosts of chemical elements: A review, *Int. J. Coal Geology*, 212, 103251, 2019.
 Fischer, R., Zekert, N., and Takeshita, N.: Polarized growth in fungi – interplay between the cycloskeleton, positional markers and membrane domains, *Molec. Microbiol.*, 68, 813-826, 2008.
 Franz, G., Khomenko, V., Vishnyevskyy, A., Wirth, R., Nissen, J., Rocholl A.: Biologically mediated crystallization of buddingtonite in the Paleoproterozoic: Organic-igneous interactions from the Volyn pegmatite, Ukraine, *Amer. Mineral.* 102, 2119-2135, 2017.
 Franz, G., Lyckberg, P., Khomenko, V., Chournousenko, V., Schulz, H.-M., Mahlstedt, N., Wirth, R., Glodny, J., Gernert, U., and Nissen, N.: Fossilization of Precambrian organic matter (kerite) from the Volyn pegmatite, Ukraine, *BioGeosci.*, 19, 1795-1811, 2022a.
 Franz, G., Sudo, M., Khomenko, V.: ⁴⁰Ar/³⁹Ar dating of a hydrothermal pegmatitic buddingtonite-muscovite assemblage from Volyn, Ukraine, *Eur. J. Mineral.*, 34, 7-18, 2022b. doi.org/10.5194/ejm-34-7-2022.
 Gan, T., Luo, T., Pang, K., Zhou, Ch., Zhou, G., Wan, B., Li, G., Yi, Q., Czaja, A. D. and Xiao, S.: Cryptic terrestrial fungus-like fossils of the early Ediacaran Period, *Nature Comm.*, doi.org/10.1038/s41467-021-20975-1, 2021.
 Gibson, T. M., Shih, P. M., Cumming, V. M., Fischer, W. W., Crockford, P. W., Hdgekiss, M. S. W., Wörendle, S., Creaser, R. A., Rainbird, R. H., Skulski, T. M., and Halverson, G. P.: Precise age of *Bangiomorpha pubescens* dates the origin of eukaryotic photosynthesis, *Geology*, 46, 135-138, 2018.
 Ginzburg, A.I., Bulgakov, V.S., Vasilishin, I.S., Luk'yanova, V.T., Solntseva, L.S., Urmenova, A.M., and Uspenskaya, V.A.: Kerite from pegmatites of Volyn, *Dokl. Akad. Nauk SSSR*, 292, 188–191, 1987, (in Russian).
 Gorlenko, V.M., Zhmur, S.I., Duda, V.I., Osipov, G.A., Suzina, N.E., and Dmitriev, V. V.: Fine structure of fossilized bacteria in Volyn kerite, *Orig. Life Evol. Biosph.*, 30, 567–577, 2000.
 Gorokov, I. M., Clauer, N., Varshavskaya, E. S., Kutyavin, E. P., and Drannik, A. S.: Rb-Sr ages of Precambrian sediments from the Ovruch Mountain range, Northwestern Ukraine (U.S.S.R.), *Precam. Res.*, 6, 55-65, 1981.
 Hall-Stoodley, L., Costerton, J. W., and Stoodley, P.: Bacterial biofilms: From the natural environment to infectious diseases, *Nature Rev. Microbiol.*, 2, 95-108, 2004.
 Högberg, P., Plamboeck, A. H., Taylor, A. F. S., and Fransson, P. M. A.: Natural ¹³C abundance reveals trophic status of fungi and host-origin of carbon in mycorrhizal fungi in mixed forests, *Proc. Natl. Acad. Sci. USA*, 96, 8534-8539, 1999.
 Ivanovich, P. V., and Alekseevich, D. S.: Mineralogy of the Volynian chamber pegmatites, *EKOST Association, Mineral. Almanac*, 12, 128 p, Moscow, 2007.

Formatiert: Englisch (USA)

Krings, M., Taylor, T. N., and Dotzler, N.: Fossil evidence of the zygomycetous fungi, *Persoonia*, 30, 1-10, 2013.
 Lepot, K., Williford, K. H., Ushikubo, T., Sugitani, K., Mimura, K., Spicuzza, M. J., and Valley, J. W.: Texture-specific isotopic compositions in 3.4 Gyr old organic matter support selective preservation in cell-like structures, *Geochim. Cosmochim. Acta*, 112, 66-86, 2013.
 Li J., Zhang L.-P., Peng F., Bian J., Yuan T.-Q., Xu F., Sun R.-C.: Microwave-assisted solvent-free acetylation of cellulose with acetic anhydride in the presence of iodine as a catalyst, *Molecules*, 14, 3551-3566, 2009. doi:10.3390/molecules14093551.
 Liang, X., Perez, M. A. M.-J., Nwoko, K. C., Egbers, P., Feldmann, J., Csentyi, L., and Gadd, G. M.: Fungal formation of selenium and tellurium nanopartikels, *Appl. Microbiol. Biotechn.*, 103, 7241-7259, 2019.
 Liang, X., Perez, M. A. M.-J., Zhang, S., Song, W., Armstrong, J. G., Bullock, L. A., Feldmann, J., Parnell, J., Csentyi, L., and Gadd, G. M.: Fungal transformation of selenium and tellurium located in a volcanogenic sulfide deposit, *Environ. Microbiol.*, 22, 2346-2364, 2020.
 Loron, C. C., François, C., Rainbird, R. H., Turner, E. C., Borensztajn, S., and Javaux, E. J.: Early fungi from the Proterozoic era in Arctic Canada, *Nature*, 370, 7760: 232-235, 1992.
 Lu'kyanova, V. T., Lobzova, R. V., and Popov, V. T.: Filaceous kerite in pegmatites of Volyn, *Izvestiya Ross. Akad. Nauk Ser. Geologicheskaya*, 5, 102-118 (in Russian), 1002.
 Lutzoni, François, Michael D. Nowak, Michael E. Alfaro, Valérie Reeb, Jolanta Miadlikowska, Michael Krug, A. Elizabeth Arnold et al.: Contemporaneous radiations of fungi and plants linked to symbiosis, *Nature Comm.* 9, no. 1, 1-11, 2018.
 Lyckberg, P., Chornousenko, V., and Wilson, W. E.: Famous mineral localities: Volodarsk-Volynski, Zhitomir Oblast, Ukraine, *The Mineral. Record*, 40, 473-506, 2009.
 Lyckberg, P., Chournousenko, V., and Chournousenko, O.: Giant heliodor and topaz pockets of the Volodarsk chamber pegmatites, Korosten pluton, Ukraine, 36th Intern. Gemm. Conf., Nantes, France, Abstr. vol., 78-83, 2019.
 McMahon, S.: Earth's earliest and deepest purported fossils may be iron-mineralized chemical gardens, *Proceedings of the Royal Society, B* 286, 2018.
<http://dx.doi.org/10.1098/rspb.2019.2410>.
 Mariotti, A.: Atmospheric nitrogen is a reliable standard for natural ¹⁵N abundance measurements, *Nature*, 303(5919), 685-687, 1983.
 Mayor, J. R., Schuur, E. A. G., and Henkel, T. W.: Elucidating the nutritional dynamics of fungi using stable isotopes, *Ecology Lett.*, 12, 171-183, 2009.
 Matusyak, D. M.: Radiotolerant microorganisms – characterization of selected species and their potential usage, *Adv. Microbiol.*, 55, 182-194, 2016.
 Miao, L. Y., Moczyłowska, M., Zhu, S. X. and Zhu, M. Y.: New record of organic-walled, morphologically distinct microfossils from the late Paleoproterozoic Changcheng Group in the Yanshan Range, North China, *Precam. Res.*, 321, 172-198, 2019.
 Missen, O. P., Ram, R., Mills, S. J., Etschmann, B., Reith, F., Shuster, J., Smith, D., J., and Brugger, J.: Love is in the Earth: A review of tellurium (bio)geochemistry in surface environments, *Earth Sci. Rev.*, 2020, doi.org/10.1016/j.earthscirev.2020.103150.
 Morais, L., Fairchild, T. R., Lahr, D. J. G., Rudnitski, I. D., Schopf, J. W., Garcia, A. K., Kudryavtsev, A. B., and Romero, G. R.: Carbonaceous and siliceous Neoproterozoic vase-shaped microfossils (Urucum Formation, Brazil) and the question of early protistan biomineralization, *J. Paleontol.*, 91(3), 393-406, 2017. doi: 10.1017/jpa.2017.16.
 Nakamoto K.: Infrared spectra of inorganic and coordination compounds, Parts A and B. New York: Wiley, p. 328., John Wiley & Sons, New York, 1997.
 Nims, C., Lafond, J., Alleon, J., Templeton, A. S., and Cosmidis, J.: Organic biomorphs may be better preserved than microorganisms in the early Earth sediments, *Geology*, 49, 629-634, 2021. <https://doi.org/10.1130/G48152.1>.

Gelöscht: Levin, L. A., and Michener, R.: Isotopic evidence of chemosynthesis-based nutrition of macrobenthos: The lightness of being at Pacific methane seeps, *Limnol. Oceanogr.*, 47, 1336-1345, 2002.

Formatiert: Durchgestrichen

Formatiert: Englisch (USA)

Petersen, B. M., and Fry, B.: Stable isotopes in ecosystem studies, *Ann. Rev. Ecology System.*, 18, 293-320, 1987.

Prothman, C., and Zauner, K.-P. Semibiotic Persistence, *J. Brit. Interplanet. Soc. (JBIS)*, 67(7-9), 314-321, 2014 doi://www.jbis.org.uk/paper.php?p=2014.67.314.

Rasmussen, B., Blake, T. S., Fletcher, I. R., and Kilbum, M. R.: Evidence for microbial life in synsedimentary cavities from 2.75 Ga terrestrial environments, *Geology*, 37, 423-426, 2009.

Rikkinen, J., Grimaldi, D. A., and Schmidt, A.: Morphological stasis in the first myxomycete from the Mesozoic, and the likely role of cryptobiosis, *Scientific Reports* 9.1, 19730, 2019.

Roulliard, J., Garcia-Ruiz, J.-M., Gong, J., and van Zuilen, M. A.: A morphogram for siliawitherite biomorphs and its application to microfossil identification in the early earth rock record, *Geobiology*, 16, 279-296, 2018. <https://doi.org/10.1111/gbi.12278>.

Schnittler, M., Novozhilov, Y. K., Romeralo, M., Brown, M., and Spiegel, F. W.: Fruit body-forming protists: Myxomycetes and Myxomycete-like organisms, chapter 4, 40-88, in: Engler, A., and Frey, W., *Syllabus of Plant Families-A. Engler's Syllabus der Pflanzenfamilien Part 1/1*, Stuttgart: Bornträger, 2012.

Sergeev, V. N., and Schopf, J. W.: Taxonomy, paleoecology and biostratigraphy of the Late Neoproterozoic Chichkan microbiota of South Kazakhstan: The marine biosphere on the eve of metazoan radiation, *J Paleont.*, 84, 363-401, 2010

Shourie, A., and Vijayalakshmi U.: Fungal diversity and its role in mycoremediation, *Geomicrobiol. J.*, 39, 3-5, 426-444, 2022, doi: [10.1080/01490451.2022.2032883](https://doi.org/10.1080/01490451.2022.2032883)

Shumlyanskyy, L., Billström, K., Hawkesworth, C., and Elming, S.-Å.: U-Pb age and Hf isotope compositions of zircons from the north-western region of the Ukrainian shield: mantle melting in response to post-collision extension. *Terra Nova* 24, 373-379, 2012.

Shumlyanskyy L., Hawkesworth C., Billström K., Bogdanova S., Mytrokhyn O., Romer R., Dhuime B., Claesson S., Ernst R., Whitehouse M., Bilan O.: The origin of the Palaeoproterozoic AMCG complexes in the Ukrainian Shield: new U-Pb ages and Hf isotopes in zircon, *Precam. Res.*, 292, 216-239, 2017.

Shumlyanskyy, L., Franz, G., Glynn, S., Mytrokhyn, O., Voznyak, D., and Bilan O.: Geochronology of granites of the western part of the Korosten AMCG complex (Ukrainian Shield): implications for the emplacement history and origin of miarolitic pegmatites, *Eur. J. Min.*, 33, 703-716, 2021.

Stephenson, S. L., Schnittler, M., and Nvozhilov, Y. K.: Myxomycete diversity and distribution from the fossil record to the present, *Biodivers. Conserv.*, 17, 285-301, 2008. Doi: [10.1007/s10531-007-9252-9](https://doi.org/10.1007/s10531-007-9252-9).

Stephenson, S. L., and Schnittler, M., Myxomycetes, in: Archibald et al. (eds.) *Handbook of the protists*, 1-26, Springer International Publishing AG 2016. Doi [10.1007/978-3-319-32660-6_44-1](https://doi.org/10.1007/978-3-319-32660-6_44-1).

Struck, U.: On the use of stable nitrogen isotopes in present and past anoxic environments. In: Altenbach, A. V., Bernard, J. M. and Seckbach, J. (eds.) *Anoxia, evidence for eukaryote survival and paleontological strategies*. Book series: Cellular origin, life in extreme habitats and astrobiology, 21, 497-513, Springer, Berlin, 2012.

Tugay, T., Zhdanova, N.N., Zheltonozhsky, V., Sadovnikov, L., and Dighton, J.: The influence of ionizing radiation on spore germination and emergent hyphal growth response reactions of microfungi, *Mycologia*, 98, 4, 521-527, 2006/2017. doi: [10.1080/15572536.2006.11832654](https://doi.org/10.1080/15572536.2006.11832654).

Vasilev, A., Efimov, M., Bondarenko, G., Kozlov, V., Dzidziguri, E., and Karpacheva, G.: Thermal behavior of chitosan as a carbon material precursor under IR radiation, *IOP Conf. Ser.: Mater. Sci. Eng.* 693, 2019, <https://doi.org/10.1088/1757-899X/693/1/012002>.

Volland, J.-M., Gonzalez-Rizzo, S., Gros, O., Tymb, T., Ivanova, N., Schulz, F., Goudeau, D. et al.: A centimeter-long bacterium with DNA contained in metabolically active, membrane-bound organelles. *Science*, 376.6600, 1453-1458, 2022. doi: [10.1126/science.abb3634](https://doi.org/10.1126/science.abb3634).

Gelöscht: Peterson, B.J., and Fry, B.: Stable isotopes in ecosystem studies, *Ann. Rev. Ecol. Syst.*, 18, 293-320, 1987.

Formatiert: Durchgestrichen

Gelöscht: Rau, G. H., Teyssie, J. L., Tassoulzadegan, R., and Rowler, S. W.: $^{13}\text{C}/^{12}\text{C}$ and $^{15}\text{N}/^{14}\text{N}$ variations among size-fractionated marine particles: implication for their origin and trophic relationships, *Marine Ecol. Progr. Ser.*, 59, 33-38, 1990.

Rau, G. H., Riebesell, U., and Wolf-Gladrow, D. A.: A model of photosynthetic ^{13}C fractionation by marine phytoplankton based on diffusive molecular CO_2 uptake, *Marine Ecol. Progr. Ser.*, 133, 275-285, 1996

Formatiert: Nicht Durchgestrichen

Formatiert: Englisch (USA)

Formatiert: Englisch (USA)

Gelöscht: -

Formatiert: Durchgestrichen

Formatiert: Links, Abstand zwischen asiatischem und westlichem Text anpassen, Abstand zwischen asiatischem Text und Zahlen anpassen

Formatiert: Englisch (USA)

Formatiert: Englisch (USA)

Formatiert: Englisch (USA)

Formatiert: Englisch (USA)

Formatiert: Englisch (USA)

Formatiert: Englisch (USA)

Feldfunktion geändert

Formatiert: Englisch (USA)

Formatiert: Englisch (USA)

Formatiert: Englisch (USA)

Feldfunktion geändert

Feldfunktion geändert

Feldfunktion geändert

1088 Wanjun T., Cunxin W., Donghua, C.: Kinetic studies on the pyrolysis of chitin and chitosan,
 1089 Polym. Degrad. Stabil. 87, 389–394, 2005.
 1090 Wang, D. Y.-C., Kumar, S., and Hedges, S. B.: Divergence time estimates for the early history
 1091 of animal phyla and the origin of plants, animals and fungi, Proc. R. Soc. Lond., 266, 163-171,
 1092 1999.
 1093 Wellman, C. H., and Strother, P. K.: The terrestrial biota prior to the origin of land plants
 1094 (embryophytes): A review of the evidence, Paleontol., 58, 601-627, 2015.
 1095 Westall, F., de Witt, M. J., Dann, J., van der Gaast, S. de Ronde, C. E.J., and Gerneke, D.: Early
 1096 Archean fossil bacteria and biofilms in hydrothermally-influenced sediments from the
 1097 Barberton greenstone belt, South Africa. Prec. Res., 106, 93-116, 2001.
 1098 Zawadzki, J., and Kaczmarek, H.: Thermal treatment of chitosan in various conditions,
 1099 Carbohydr. Polym., 80, 394-400, 2010.
 1100 Zhmur, S. I.: Origin of Cambrian fibrous kerites of the Volyn region, Lithol. Mineral Resour.,
 1101 38, 55-73, 2003.